Supporting Information for the manuscript:

# Broad-band spectroscopy of a vanadyl porphyrin: a model electronuclear spin qudit

Ignacio Gimeno, Ainhoa Urtizberea, Juan Román-Roche, David Zueco, Agustín Camón, Pablo J. Alonso, Olivier Roubeau,* and Fernando Luis*

## Table of contents

## Synthesis

Commercial 5,10,15,20-tetrakis(4-carboxyphenyl)porphine ($H_6TCPP$, >97%) was purchased from TCI. $VO(SO_4)\cdot H_2O$ (>99.0%), Ti(IV)oxysulfate (>29% Ti as $TiO_2$ basis), were purchased from Aldrich and used without further purification.

**Synthesis of [VO(TCPPEt)] ($\mathbf{1^{VO}}$).** This was done as previously reported,[1] under conditions that were used before for the Cu analogue.[2] $H_6TCPP$ (81 mg, 0.10 mmol), $VO(SO_4)\cdot H_2O$ (17 mg, 0.094 mmol) and 10 mL ethanol were gently mixed in a 23 mL Teflon-lined PARR acid digestion bomb, and the operation repeated 5 times. The five bombs were placed in an oven at 60ºC, warmed to 180ºC and kept at this temperature for 24 h. After cooling to RT, large shiny violet crystals were recovered by filtration, washed with little ethanol and dried in air. The total yield of crystals of $\mathbf{1^{VO}}$ was 422 mg (77% based on V, 0.436 mmol). MALDI-TOF-MS (matrix: CHCA): m/z = 967.6. EA calc. (found) for $C_{56}H_{44}N_4O_9V$: C, 69.49 (69.2); H, 4.58 (4.5); N, 5.79 (5.6) wt%.

**Synthesis of $\mathbf{[(TiO)_{(1-x)}(H_{2x}TCPPEt)]}$ ($\mathbf{1^{TiO}}$).** $H_6TCPP$ (84 mg, 0.104 mmol), $TiO(SO_4)\cdot xH_2O$ (24 mg, 0.139 mmol considering x = 1) and 10 mL ethanol were gently mixed in a 23 mL Teflon-lined PARR acid digestion bomb, and the bomb was placed in an oven at 60ºC, warmed to 180ºC and kept at this temperature for 24 h. After cooling to RT, large shiny violet crystals were recovered by filtration, washed with little ethanol and dried in air. The total yield of crystals of $\mathbf{1^{TiO}}$ was 68 mg. Repeated reactions systematically gave crystals with only a partial metallation. The Ti content determined through ICP-MS was reproducibly corresponding to x ranging from 0.4 to 0.6, in agreement with repeated single-crystal structure refinements. The reported structure for $\mathbf{1^{TiO}}$ refines to x = 0.5. We did not find any crystal of the free-base $H_2TCPPEt$ over 20+ single-crystals tested.
The same reaction was repeated with increasing excess of $TiO(SO_4)\cdot xH_2O$ up to *ca.* 5-fold excess (103 mg, 0.506 mmol considering x = 1), resulting in a mixture of large violet crystals and an increasing amount of white solid, found to be unreacted $TiO(SO_4)\cdot xH_2O$ based on IR spectra. The violet crystals were found to be either crystals of $\mathbf{1^{TiO}}$, still with x of the order of 0.5 or crystals of the free-base $H_2TCPPEt$, from which the reported structure was determined.

**Synthesis of $\mathbf{[(VO)_{0.03}(TiO)_{0.53}(H_2)_{0.44}TCPPEt)]}$ ($\mathbf{1^{VO}_{3\%}}$).** The synthesis was done as for $\mathbf{1^{TiO}}$ albeit using $H_6TCPP$ (83 mg, 0.103 mmol), $VO(SO_4)\cdot H_2O$ (0.6 mg, 0.003 mmol) and $TiO(SO_4)\cdot xH_2O$ (20.3 mg, 0.118 mmol considering x = 1). Large shiny violet crystals were recovered by filtration, washed with little ethanol and dried in air. The total yield of crystals of $\mathbf{1^{VO}_{3\%}}$ was 75 mg. Single-crystal X-ray diffraction repeatedly gave a unit-cell very close to that found for $\mathbf{1^{TiO}}$ (see Table S1). The average metal composition was determined by ICP-MS. As expected from the outcome of the synthesis of $\mathbf{1^{TiO}}$, metallation by the titanyl ion is not complete and the crystals are a mixture of vanadyl, titanyl and unmetallated porphyrins. Each crystal likely has a slightly different composition.

**Synthesis of $\mathbf{H_2TCPPEt}$.** $H_6TCPP$ (84 mg, 0.104 mmol) and 10 mL ethanol were gently mixed in a 23 mL Teflon-lined PARR acid digestion bomb, and the bomb was placed in an oven at 60ºC, warmed to 180ºC and kept at this temperature for 24 h. After cooling to RT, a violet polycrystalline powder was recovered by filtration, washed with little ethanol and dried in air. The total yield of $H_2TCPPEt$ was 58 mg. No large single-crystal were obtained,

---

[1] A. Urtizberea, E. Natividad, P. J. Alonso, L. Pérez, M. A. Andrés, I. Gascón, I. Gimeno, F. Luis, O. Roubeau, *Mater. Horiz.*, **2020**, 7, 885.

[2] W. Chen, and S. Fukuzumi, *Eur. J. Inorg. Chem.*, **2009**, 5494.

and attempts to obtain large single-crystals of $[(VO)_x(H_2)_{2-2x}TCPPEt]$ also only yielded polycrystalline powders.

## Single-Crystal X-Ray Crystallography (SCXRD)

Data for $H_2TCPPEt$ were acquired at 100 K on a 0.20x0.17x0.16 $mm^3$ violet block on a Bruker APEX II QUAZAR diffractometer equipped with a microfocus multilayer monochromator with MoK$\alpha$ radiation ($\lambda$ = 0.71073 Å). Data reduction and absorption corrections were performed with respectively SAINT and SADABS.[3] Data for $\mathbf{1}^{\mathbf{VO}}$ and $\mathbf{1}^{\mathbf{TiO}}$ were obtained respectively on a 0.88x0.47x0.19 $mm^3$ violet block at 150 K and on a 0.22x0.06x0.03 $mm^3$ violet lath at 295 K on an Oxford Diffraction Excalibur Sapphire3 diffractometer with enhanced MoK$\alpha$ radiation ($\lambda$ = 0.71073 Å), at the X-ray diffraction and Fluorescence Analysis Service of the University of Zaragoza. Cell refinement, data reduction, and absorption corrections were performed with the CrysAlisPro suite.[4] All structures were solved by intrinsic phasing with SHELXT[5] and refined by full-matrix least-squares on $F^2$ with SHELXL-2014.[6] All details can be found in CCDC 2058759-2058760-2058761 ($H_2TCPPEt$-$\mathbf{1}^{\mathbf{VO}}$-$\mathbf{1}^{\mathbf{TiO}}$) that contain the supplementary crystallographic data for this paper. These data can be obtained free of charge from The Cambridge Crystallographic Data Center via https://summary.ccdc.cam.ac.uk/structure-summary-form. Crystallographic and refinement parameters are summarized in Table S1**.** Selected bond lengths and angles and intermolecular distances are given in Tables S2 and S3.

**Electron Paramagnetic Resonance (EPR)** experiments, both continuous wave (CW) and pulsed time domain (TD), were performed with a Bruker Biospin ELEXSYS E-580 spectrometer operating in the X-band, using a gas-flow Helium cryostat for low-temperature experiments. Rotational CW studies were on single-crystals of both $\mathbf{1}^{\mathbf{VO}}$ and $\mathbf{1}^{\mathbf{VO}}_{\mathbf{3\%}}$ mounted on 2x2x2 $mm^3$ cube-shaped holder (see Figure S3). TD experiments were done on a frozen solution $\mathbf{1}^{\mathbf{VO}}_{\mathbf{sol}}$ (0.46 mmol/L $\mathbf{1}^{\mathbf{VO}}$ in 1:1 mixture of toluene and $CDCl_3$) and on a single-crystal of $\mathbf{1}^{\mathbf{VO}}_{\mathbf{3\%}}$**.** 2p and Inversion Recovery ESE-detected experiments were performed. The simulated spectra were obtained with the EasySpin program.[7]

## Magnetothermal characterization

Magnetization and susceptibility data of polycrystalline $\mathbf{1}^{\mathbf{VO}}$ were measured, between 1.8 K and 300 K and for dc magnetic fields up to 5 T, with a commercial magnetometer equipped with a SQUID sensor hosted by the Physical Measurements Unit of the Servicio General de Apoyo a la Investigación-SAI, Universidad de Zaragoza. This system was also used to perform ac susceptibility measurements. For this, a sinusoidal ac magnetic field with amplitude $b_0$ = 4 Oe, oscillating at a frequency $\omega/2\pi$ between 1 Hz and 1.1 kHz, was applied parallel to the static magnetic field and the linear in-phase $\chi'$ and out-of-phase $\chi''$ susceptibility components were recorded. Additional ac susceptibility measurements were performed in the range $10 \leq \nu \leq 10000$ Hz using the ACMS option of a commercial physical property measurement system. The diamagnetic contributions to the magnetization and susceptibility were corrected using Pascal's constant tables.

Additional magnetization measurements were performed, between 0.35 K and 5 K, on a single crystal of $\mathbf{1}^{\mathbf{VO}}$ using a home-made micro-Hall magnetometer. The sample was placed on the edge of one of the three Hall crosses. A magnetic field $B < 2$ T was applied

---

[3] G. M. Sheldrick, *SAINT and SADABS*, Bruker AXS Inc.: Madison, Wisconsin, USA, 2012.

[4] *CrysAlis PRO*, Agilent Technologies Ltd, Yarnton, Oxfordshire, England.

[5] G. M. Sheldrick, *Acta Cryst. A* **2015,** *71*, 3-8.

[6] G. M. Sheldrick, *Acta Cryst. C* **2015,** *71*, 3-8.

[7] S. Stoll, A. Schweiger, *J. Magn. Reson.*, **2006**, *178*, 42.

along the plane of the sensor to minimize its intrinsic bare signal. This signal was calibrated and then subtracted from the results.

The specific heat of **$1^{VO}$** was measured, between $T$ = 0.35 K and 100 K, with a commercial physical property measurement system (PPMS, of the Servicio de Apoyo a la Investigación-SAI, Universidad de Zaragoza). A single crystal was placed onto a thin layer of apiezon N grease that fixes the sample and improves the thermal contact with the calorimeter. The PPMS makes use of the relaxation method, which measures the temperature evolution that follows after the application and subsequent removal of a heat power pulse. Experiments were performed with different durations of the pulse, to explore the dynamics in the thermalization of vanadyl spins. The raw data were corrected from the known contributions arising from the empty calorimeter and the grease.

### On-chip magnetic spectroscopy

The superconducting coplanar waveguides employed in this work consist of a 800 μm wide central transmission line separated from two ground planes by 400 μm wide gaps. They are fabricated by optical lithography on 150 nm thick Nb films ($T_C$ = 9.2 K) deposited by sputtering onto single crystalline sapphire wafers. The size of the central line and its meander shape were designed in order to best match the dimensions of the large **$1^{VO}$** single crystals used in the experiments (an optical microscopy image of a chip can be seen in Figure S26). Microwave transmission experiments were performed on a Helium cryostat ($T$ = 4.2 K) and a $^3$He-$^4$He dilution refrigerator (0.15 K < $T$ < 6 K), both of them compatible with the used 9 T × 1 T × 1 T superconducting vector magnet. The chips input and output lines were connected to a vector network analyser that measures the transmission, $S_{12}$ and $S_{21}$, and reflection, $S_{11}$ and $S_{22}$, coefficients.

The crystals were positioned onto the transmission line with Paraton N grease. The long axis of the crystals, that coincides with the crystallographic 101 axis, was oriented nearly parallel to the laboratory Z and to the axis of the device, which corresponds also to the orientation of the microwave magnetic field seen by the majority of molecules in the crystal (Figures 1 main text and S26). In order to compensate for the decay of the waveguide transmission with increasing frequency and to enhance the contrast of those effects associated with its coupling to the spins, $S_{21}$ and $S_{12}$ were normalized by a method similar to that proposed in reference 8. The normalized transmission $t$ at magnetic field $B_1$ and frequency $\omega_1$ is given by

$$t(B_1, \omega_1) = \frac{S_{21}(B_1, \omega_1) - S_{21}(B_2, \omega_1)}{S_{21}^{(0)}(\omega_1)}$$

where $B_2 > B_1$ and $S_{21}^{(0)}$is the transmission of the 'empty' transmission line. In practice, $S_{21}^{(0)}$is measured at a magnetic field for which all spin excitations are outside the accessible frequency region. For $B_2$ very close to $B_1$ (*i.e.* closer than the magnetic field width of a given absorption line), $t$ approximately corresponds to the derivative of the normalized transmission, similar to the signal detected by conventional Electron Paramagnetic Resonance (EPR) systems. The actual transmission can also be obtained by choosing $B_2$ sufficiently far from $B_1$, but at the cost of deteriorating the signal-to noise ratio.

---

[8] I. Gimeno, D. Zueco, Y. Duan, C. Sánchez-Azqueta, T. Astner, A. Gaita-Ariño, S. Hill, J. Majer, E. Coronado and F. Luis, arXiv:1911.07541

**Table S1.** Crystallographic and refinement parameters for the structures of $\mathbf{1}^{\mathbf{VO}}$, $\mathbf{1}^{\mathbf{TiO}}$ and $H_2$TCPPEt. A representative example of the unit-cells obtained for $\mathbf{1}^{\mathbf{VO}}_{\mathbf{3\%}}$ is given for comparison**.**

| Compound | $\mathbf{1}^{\mathbf{VO}}$ | $\mathbf{1}^{\mathbf{TiO}}$ | $\mathbf{1}^{\mathbf{VO}}_{\mathbf{3\%}}$ | $H_2$TCPPEt |
|---|---|---|---|---|
| Formula | $C_{56}H_{44}N_4O_9V$ | $C_{56}H_{44}N_4O_{8.5}Ti0.5$ | | $C_{56}H_{46}N_4O_8$ |
| FW (g mol$^{-1}$) | 967.89 | 933.91 | | 902.97 |
| Wavelength (Å) | 0.71073 | 0.71073 | 0.71073 | 0.71073 |
| $T$ (K) | 150(2) | 295(2) | 295(2) | 100(2) |
| Crystal system | monoclinic | monoclinic | monoclinic | monoclinic |
| Space group | $P2_1$/n | $P2_1$/n | | $P2_1$/n |
| $a$ (Å) | 9.3937(6) | 9.4036(14) | 9.393(3) | 9.0183(15) |
| $b$ (Å) | 10.8559(6) | 10.8957(13) | 10.878(3) | 10.8486(18) |
| $c$ (Å) | 22.317(2) | 22.319(3) | 22.319(6) | 22.331(3) |
| $\beta$ (°) | 93.508(8) | 90.524(13) | 90.73(3) | 92.992(9) |
| $V$ (Å$^3$) | 2271.6(3) | 2286.7(5) | 2280(2) | 2181.8(6) |
| $Z$ | 2 | 2 | | 2 |
| $\rho_{\mathrm{calcd}}$ (g cm$^{-3}$) | 1.415 | 1.356 | | 1.374 |
| $\mu$ (mm$^{-1}$) | 0.285 | 0.171 | | 0.093 |
| Reflections | 3997 | 1359 | | 3693 |
| $R_{\mathrm{int}}$ | 0.0434 | 0.0664 | | 0.0291 |
| Restraints | 156 | 7 | | 17 |
| Parameters | 385 | 324 | | 326 |
| $S$ | 1.029 | 1.016 | | 1.132 |
| $R_1$ [$I$>2$\sigma$($I$)] | 0.0895 | 0.0672 | | 0.0601 |
| w$R_2$ [$I$>2$\sigma$($I$)] | 0.2274 | 0.1724 | | 0.1536 |
| $R_1$ [all data] | 0.1210 | 0.1054 | | 0.0660 |
| w$R_2$ [all data] | 0.2496 | 0.2071 | | 0.1573 |
| Largest peak / hole ($e$ Å$^3$) | 0.359 / –1.111 | 0.152 / –0.187 | | 0.842 / –0.389 |

**Table S2.** Details of intermolecular C–H$\cdots\pi$ and $\pi\cdots\pi$ interactions in the structure of $\mathbf{1}^{\mathbf{VO}}$ (see Figs. S1 and S2).

| pyrrole centroid | H–C | distance (Å) |
|---|---|---|
| $C_g$ (N2C7C8C9C10) | H28A–C28 | 2.755 |
| $C_g$ (N1C2C3C4C5) | H25A–C25 | 2.788 |
| | | |
| pyrrole centroid | ester pivot carbon | distance (Å) |
| $C_g$ (N2C7C8C9C10) | C17 | 3.449 |

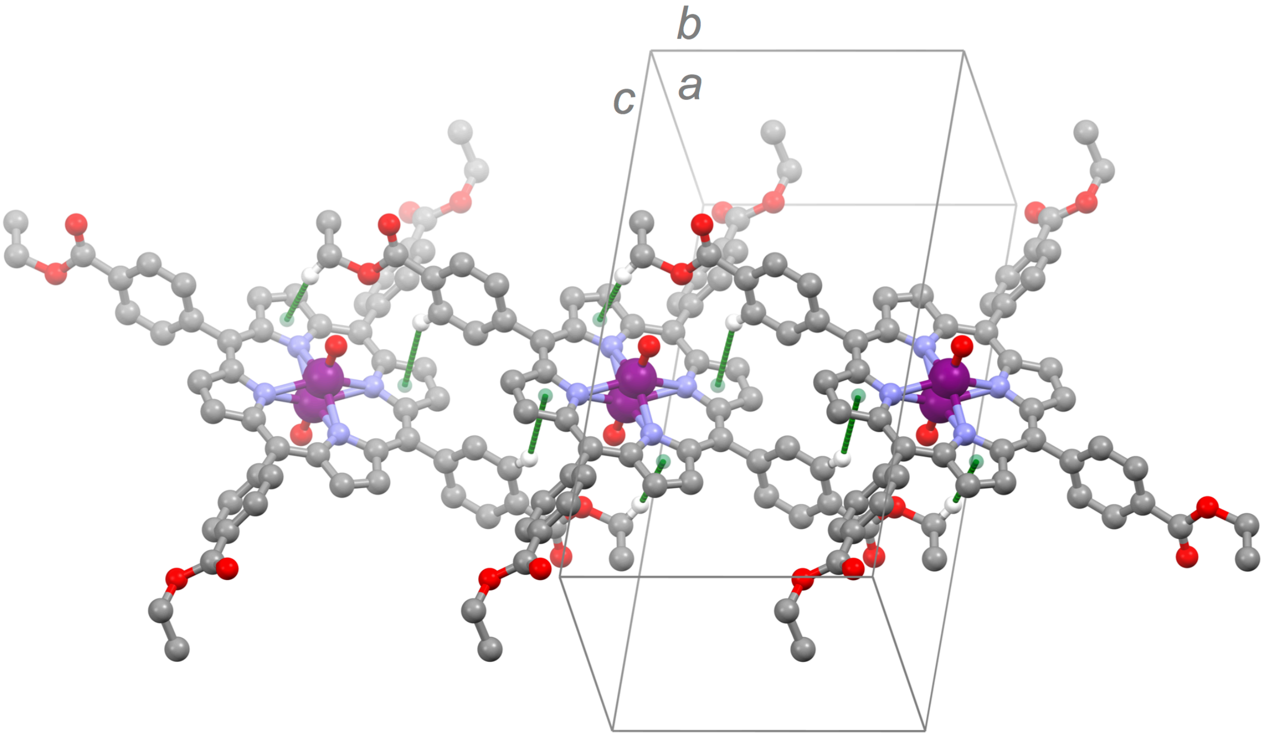

**Figure S1.** Portion of the packing in the structure of **$1^{VO}$** highlighting the intermolecular C-H···π interactions (green sticks) giving rise to supramolecular chains of [VOTCPPEt] molecules with identical orientation. Colour code: plum, V; red, O; light blue, N; grey, C, white, H, green, pyrrole rings centroids. Only hydrogens involved in the interactions are shown for clarity. See Table S2 for details.

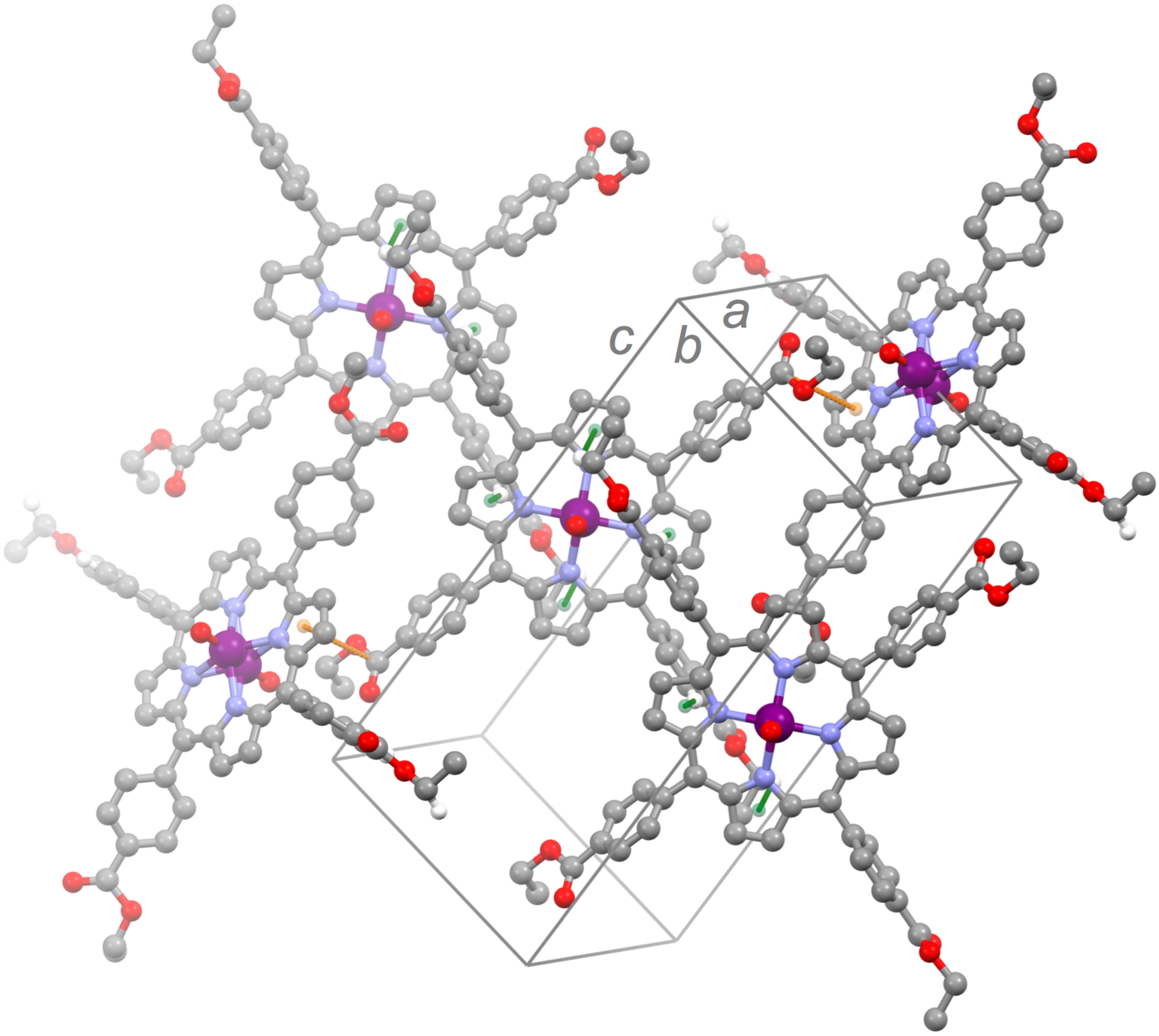

**Figure S2.** Portion of the packing in the structure of $\mathbf{1}^{\mathbf{VO}}$ highlighting the intermolecular $\pi\cdots\pi$ interactions between pyrrole rings and adjacent COO moieties (orange sticks) between [VOTCPP] molecules with different orientations. These connect the supramolecular chains (shown here is the same as in Fig. S1) in planes. Colour code: plum, V; red, O; light blue, N; grey, C, white, H, green and orange, pyrrole rings centroids. Only hydrogens involved in the C-H$\cdots\pi$ interactions (green sticks) are shown for clarity. See Table S2 for details.

**Details and analysis of single-crystal EPR measurements.**
Crystals were mounted on a “perpex” cube-shaped holder (2x2x2 mm$^3$), using GE varnish to avoid any uncontrolled modification of the crystal orientation. Figure S3a shows the crystal of $\mathbf{1}^{VO}{}_{3\%}$ on the holder after the measurements, and the definition of the laboratory axes X, Y and Z used in experiments. The Z axis coincides with the long growth direction of the crystal, the monoclinic *b* axis, while the XY plane is parallel to the glide plane. The dc magnetic field B and the microwave magnetic field $b_{mw}$ generated by the cavity were perpendicular to the rotation axis and orthogonal to each other.

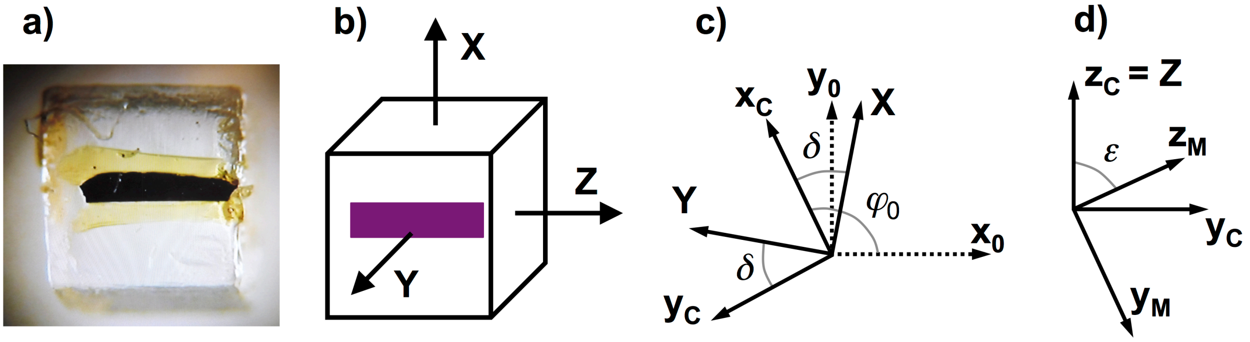

**Figure S3.** a) Picture of a crystal of mounted on a 2x2x2 mm$^3$ cube-shaped holder with a little GE varnish. b) Schematic representation of the sample orientation and definition of the XYZ laboratory axes. c) and d) Representation and relative orientations of the different reference frames used. From Fig. S5, $\varphi_0 \approx 116°$ and $\delta \approx 31°$. Considering the structural information, $\varepsilon = 64.7°$.

Spectra were first acquired for $\mathbf{1}^{VO}$ rotating 360° in 5° steps around each of the three axes defined by the cube-shaped holder X, Y, and Z. The microwave frequency hardly changed over the three series of acquisitions, being 9.8493, 9.8489 and 9.8482 GHz for rotations around X, Y and Z, respectively. Thus $\Delta\nu < 0.3$ MHz so that the frequency can be taken as constant over a full set of measurements since the resolution in magnetic field is 0.2 mT.
By convention, the reference system $(x_0, y_0, z_0)$ is introduced with $z_0 = Z$ and $x_0$ coinciding with the origin of angles for the rotation in the XY plane.
Results for rotations in the XY and YZ planes are shown in Figure 2 of the main text, and reproduced here together with the rotation in the XZ plane in Figure S4.

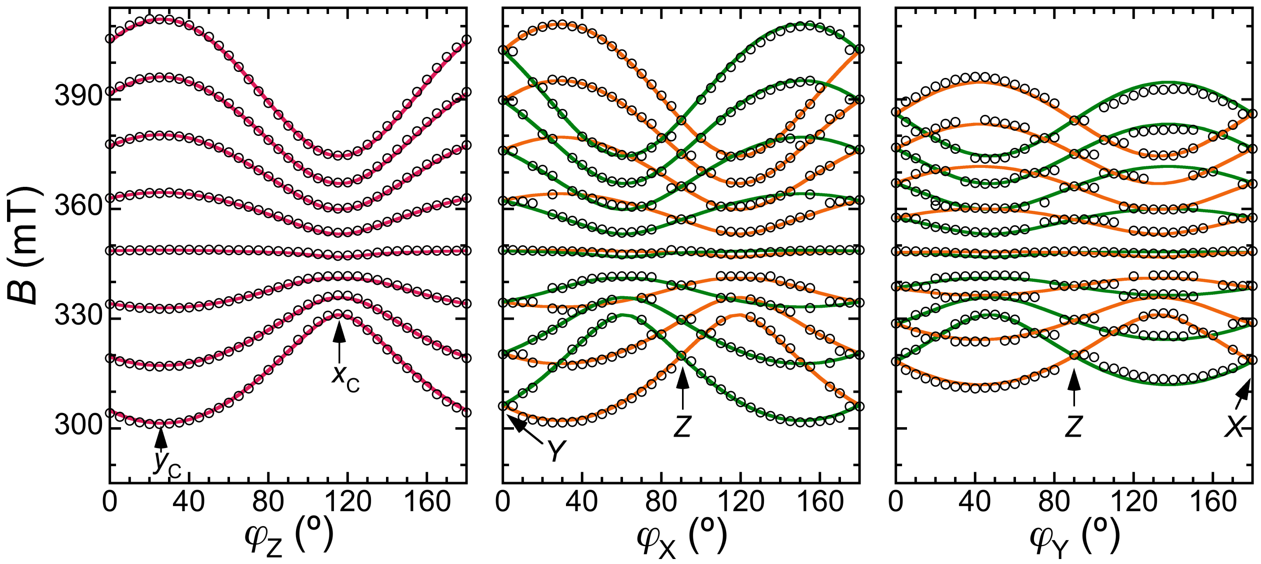

**Figure S4.** Rotational diagrams for a single crystal of **1**$^{\mathrm{VO}}$ at RT. The empty circles represent the positions of the center of the lines in the CW-EPR spectra upon rotating the crystal around the Z (left), X (middle) and Y (right) axes (see Figure S6b). Full lines are the corresponding positions calculated with the spin Hamiltonian. The contribution from the two magnetically inequivalent orientations of the molecules is represented in different colours (orange and green).

From these experiments, one can already conclude that:

i) for any orientation of the magnetic field perpendicular to the Z axis (i.e. in the XY plane), the 2 orientations of the molecules in the structure are magnetically equivalent. Thus, the rotation around the Z axis provides direct information for the molecule(s) and the symmetry of the rotational diagram exclusively reflects the molecular symmetry.

ii) there are 2 mutually perpendicular directions in the XY plane for which the total splitting of the spectrum is respectively minimal and maximal (see Figure 2 of the main manuscript). These are respectively defined as $x_C$ and $y_C$. Considering the anisotropy of the hyperfine interaction with the $^{51}$V nucleus in vanadyl complexes, $x_C$ will correspond to a direction of the XY plane perpendicular to the $z_M$ of the molecule (in principle $z_M$ corresponds to the V=O direction), and $y_C$ to the projection of $z_M$ on the XY plane (intersection of the $Zz_M$ plane with the XY plane). Then $z_C$ is defined from the $x_C$ and $y_C$ directions, parallel to Z.

iii) if the origin for angles of the rotation in the XY plane $\varphi_Z'$ is taken along $x_C$ (or $y_C$), the rotation diagram is invariant *vs.* the exchange $\varphi_Z' \rightarrow -\varphi_Z'$.

iv) the comparison of spectra measured with the magnetic field parallel to Y (rotation around X), and X (rotation around Y) with the diagram obtained by rotating around Z allows to define the positions of X and Y axes with respect to the arbitrary origins of the rotational diagram ($x_0$ and $y_0$), and relate these to $x_C$ and $y_C$ (as shown in Figures S5 and S3c).

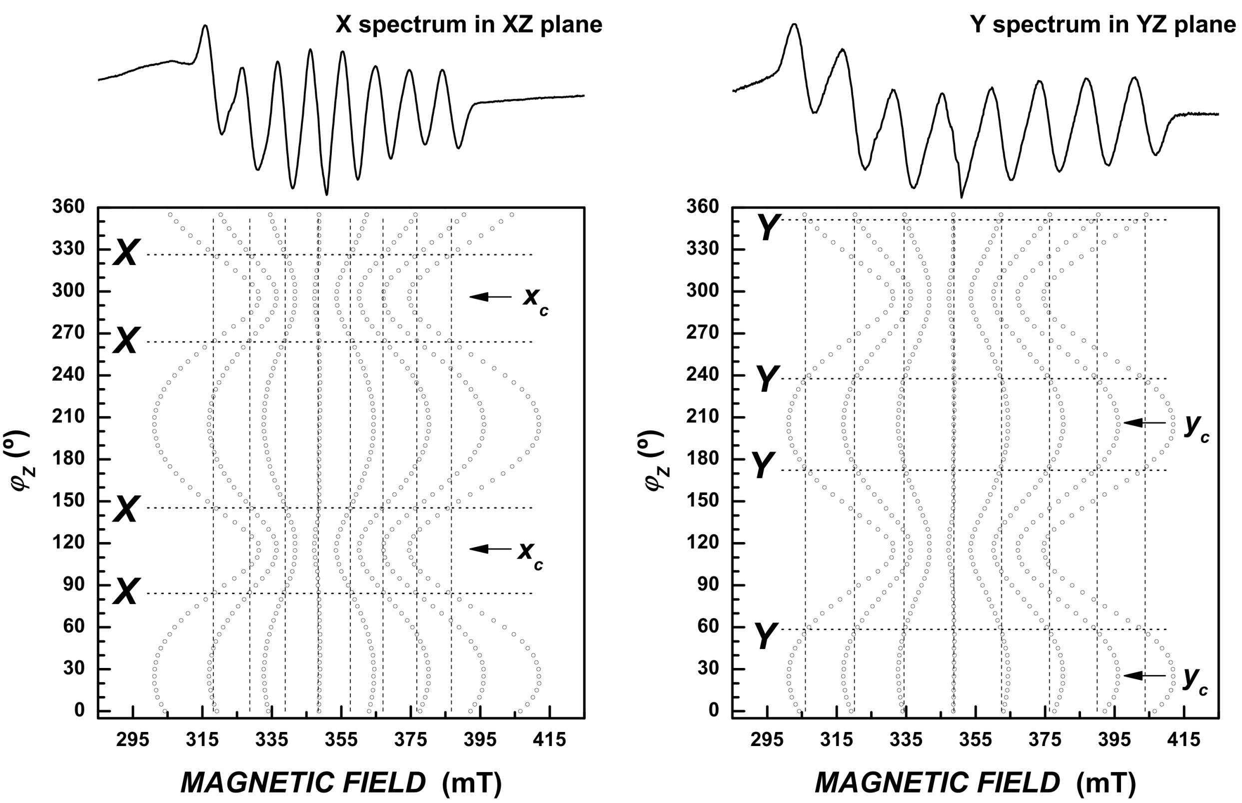

**Figure S5.** CW-EPR spectrum of a single crystal of $\mathbf{1}^{\mathbf{VO}}$ with magnetic field along the X (left) and Y (right) axis when rotating in the XZ (left) and YZ (right) plane, allowing to define the $x_C$ and $y_C$ directions, as indicated. A full spectrum is shown on the top, while the positions of the different lines are depicted in the bottom part while rotating.

The symmetry of the rotational diagram around Z indicates that $x_C$ and $y_C$ are either a $C_2$ axis or the intersection of symmetry plane with XY, the latter being equivalent to a binary axis normal to the symmetry plane from a magnetic point of view. This implies that one of the principal directions of the gyromagnetic and hyperfine tensors is along the binary axis, or normal to the symmetry plane, which can be reasoned in terms of the structure of $\mathbf{1}^{\mathbf{VO}}$. Thus, considering that $x_C$ coincides with a principal axis of both gyromagnetic and hyperfine tensors, the other two principal axis will be in the $Zy_C$ plane. Taking into account the molecular structure, one can assume an axial symmetry and define these principal axis with $z_M$ along the V=O moiety and $y_M$ being degenerate with $x_M$, which itself coincides with $x_C$. From the structural parameters, the angle $\varepsilon$ between $z_C$ (or Z) and $z_M$ should be 64.7° (Fig. S3d).

The above definitions then allow calculating the rotational dependence of the EPR spectrum, considering an axial model, for which the position of the different lines will only depend on the angle $\theta$ between the magnetic field and $z_M$. If x' is the intersection of the plane normal to the magnetic field and the plane normal to $z_M$, and defining the reference system (x', y', z') so that z' coincide with $z_M$, the spin Hamilatonian is given by:

$$H = \mu_B B(\sin\theta\, g_{\perp} S_{x'} + \cos\theta\, g_{\parallel} S_{z'}) + A_{\perp}\left(S_{x'} I_{x'} + S_{y'} I_{y'}\right) + A_{\parallel} S_{z'} I_{z'}$$

with the coordinates of unitary vector $\hat{\boldsymbol{u}}$ along $z_M$ in the reference system XYZ given by:

$$\hat{\boldsymbol{u}} = (-\sin\varepsilon \sin\delta\,,\ \sin\varepsilon \sin\delta\,,\ \cos\varepsilon)$$

Considering the generic site with $\varepsilon$, $\delta$ and $\varphi_0$ as defined above, one can determine the angle $\theta$ for the different rotations :

1) around X
with the origin of $\varphi_X$ taken as the Y axis (see Fig. S6c), the coordinates of a unitary vector in the direction of the magnetic field in the XYZ reference are [0, cos$\varphi_X$, sin$\varphi_X$] and then:

$$\cos\theta(\varphi_X) = \sin\varepsilon\cos\delta\cos\varphi_X + \cos\varepsilon\sin\varphi_X$$

2) around Y
with the origin of $\varphi_X$ taken as the X axis (see Fig. S6c), the coordinates of a unitary vector in the direction of the magnetic field in the XYZ reference are [cos$\varphi_Y$, 0, sin$\varphi_Y$] and then:

$$\cos\theta(\varphi_Y) = -\sin\varepsilon\sin\delta\cos\varphi_Y + \cos\varepsilon\sin\varphi_Y$$

3) around Z
with $\varphi_Z$ arbitrary origin taken as x0 (see Fig. S3c), the coordinates of a unitary vector in the direction of the magnetic field in the XYZ reference are [cos($\varphi_Z$–$\varphi_0$+$\delta$), sin($\varphi_Z$–$\varphi_0$+$\delta$), 0] and then:

$$\cos\theta(\varphi_Z) = \sin\varepsilon\cos(\varphi_Z - \varphi_0)$$

Although there are two magnetically inequivalent orientations of the molecules (say 1 and 2), if $\delta_1 = \delta$ and $\varphi_{01} = \varphi_0$ then $\delta_2 = \delta + \pi$ and $\varphi_{02} = \varphi_0 + \pi$, so that:

$$\cos\theta_1(\varphi_X) = \sin\varepsilon\cos\delta\cos\varphi_X + \cos\varepsilon\sin\varphi_X$$
$$\cos\theta_2(\varphi_X) = -\sin\varepsilon\cos\delta\cos\varphi_X + \cos\varepsilon\sin\varphi_X$$

$$\cos\theta_1(\varphi_Y) = -\sin\varepsilon\sin\delta\cos\varphi_Y + \cos\varepsilon\sin\varphi_Y$$
$$\cos\theta_2(\varphi_Y) = \sin\varepsilon\sin\delta\cos\varphi_Y + \cos\varepsilon\sin\varphi_Y$$

In general the angles $\theta_1$ and $\theta_2$ are different, which results in the observation of two octets in spectra for arbitrary orientations in the YZ and XZ planes. Coalescence of the two occurs for $\varphi_X = \pi/2$ or $\varphi_Y = \pi/2$ (Z direction) as well as for $\varphi_X = 0$ (Y direction) or $\varphi_Y = 0$ (X direction), since then $\theta_1 = \theta_2 = \varepsilon$ or $\theta_1 = \pi - \theta_2$ respectively. The latter situation occurs for any orientation in the XY plane (see Fig. S7).

The spin Hamiltoninan parameters were first estimated considering the spectra corresponding to situation where the magnetic field is oriented along the X, Y, Z, $x_C$ and $y_C$ directions. The spectrum of the polycrystalline sample (Fig. 2 of the main text) was also considered as it provides a good estimation of $g_\parallel$ and $A_\parallel$. On the other hand, the single-crystal spectrum with the field along $x_C$ is dominated by $g_\perp$ and $A_\perp$.
Altogether this gives:

$$g_\parallel = 1.963 \qquad g_\perp = 1.99$$

$$A_\parallel = 475\ MHz \qquad A_\perp = 172\ MHz$$

The excellent agreement between the experimental and calculated spectra is shown in Figure S6 for the five orientations mentioned above, and in Figure S7 for two intermediate orientations. Figure S4 and Fig. 2 of the main text show a good agreement with the positions of the different resonance lines (when sufficiently resolved) for the three rotational diagrams. Figure S8 illustrates the agreement between theory and experimental results using a 2D diagram built from all spectra. For rotations in the XZ and YZ planes, the contribution from the two inequivalent orientations are marked with different colours. There is only a small disagreement for the outer lines measured in the XZ plane, which we ascribe to a small misalignement of the cube-shaped holder as it was placed onto the main sample holder.

The same procedure was applied for $\mathbf{1}^{\mathrm{VO}}_{3\%}$, for which the data obtained are virtually identical, as the same spin Hamiltonian parameters are able to reproduce the experimental spectra and the positions of all resonance lines (see Figure 5 of the main text and Figure S9). There is however an additional isotropic signal at g = 2.01 in all spectra, which we ascribe to a Ti(III) impurity. Some disagreement is also observed between the experimental and calculated angle dependence for the rotation in the XZ plane, which we again ascribe to a small error in the alignment of the cube-shaped holder.

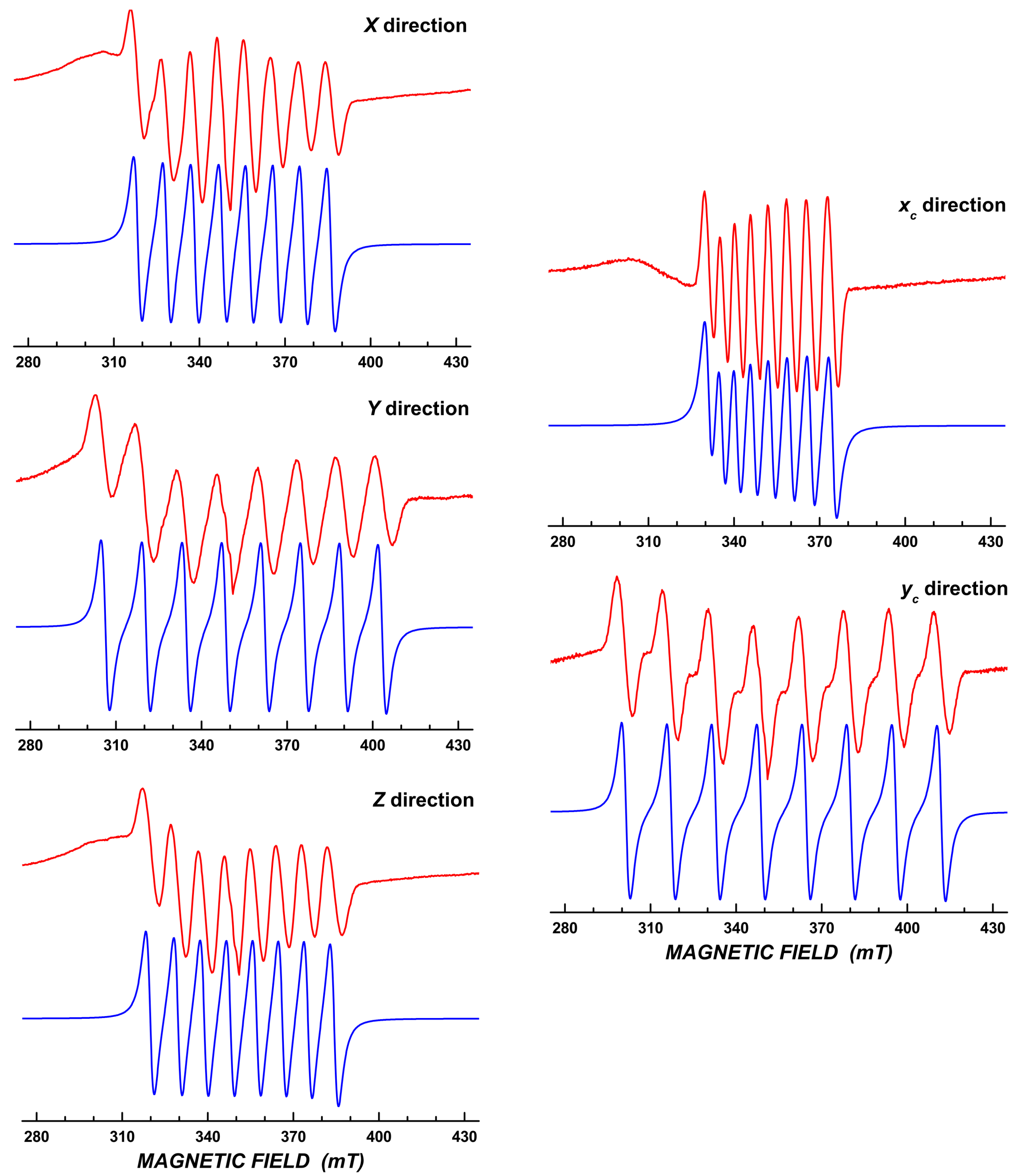

**Figure S6.** Comparison of experimental (red lines) and calculated (blue lines) CW-EPR spectra of a single crystal of $\mathbf{1}^{\mathrm{VO}}$ with the magnetic field along the indicated directions. Calculated spectra were obtained using a Lorentzian lineshape with a 3 mT isotropic width.

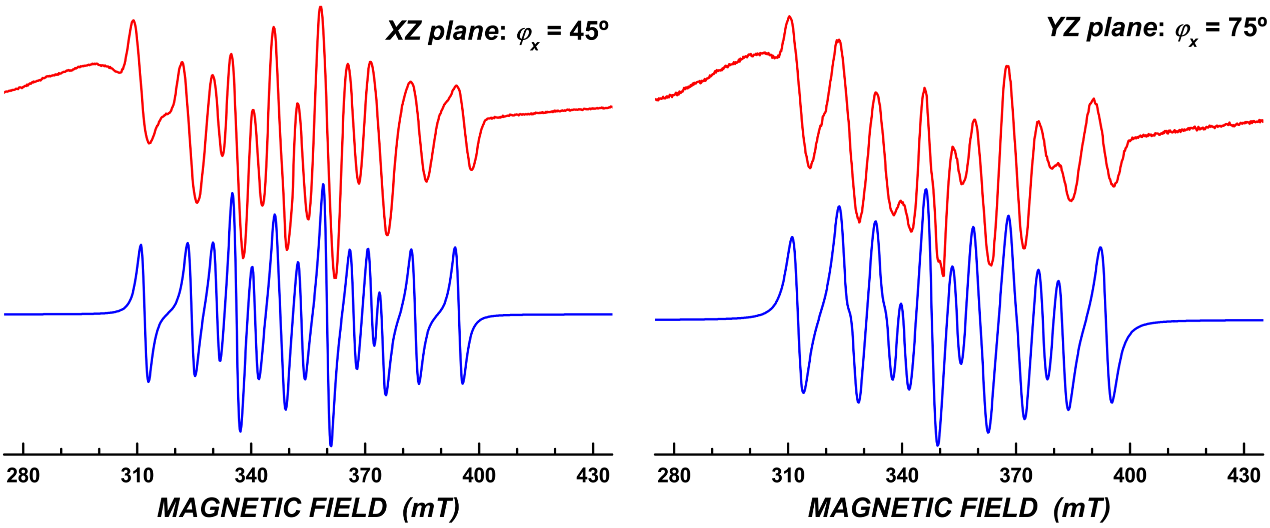

**Figure S7.** Comparison of experimental (red lines) and calculated (blue lines) CW-EPR spectra of a single crystal of $\mathbf{1}^{\mathrm{VO}}$ with the magnetic field along the indicated directions. Calculated spectra were obtained using a Lorentzian lineshape with a 3 mT isotropic width.

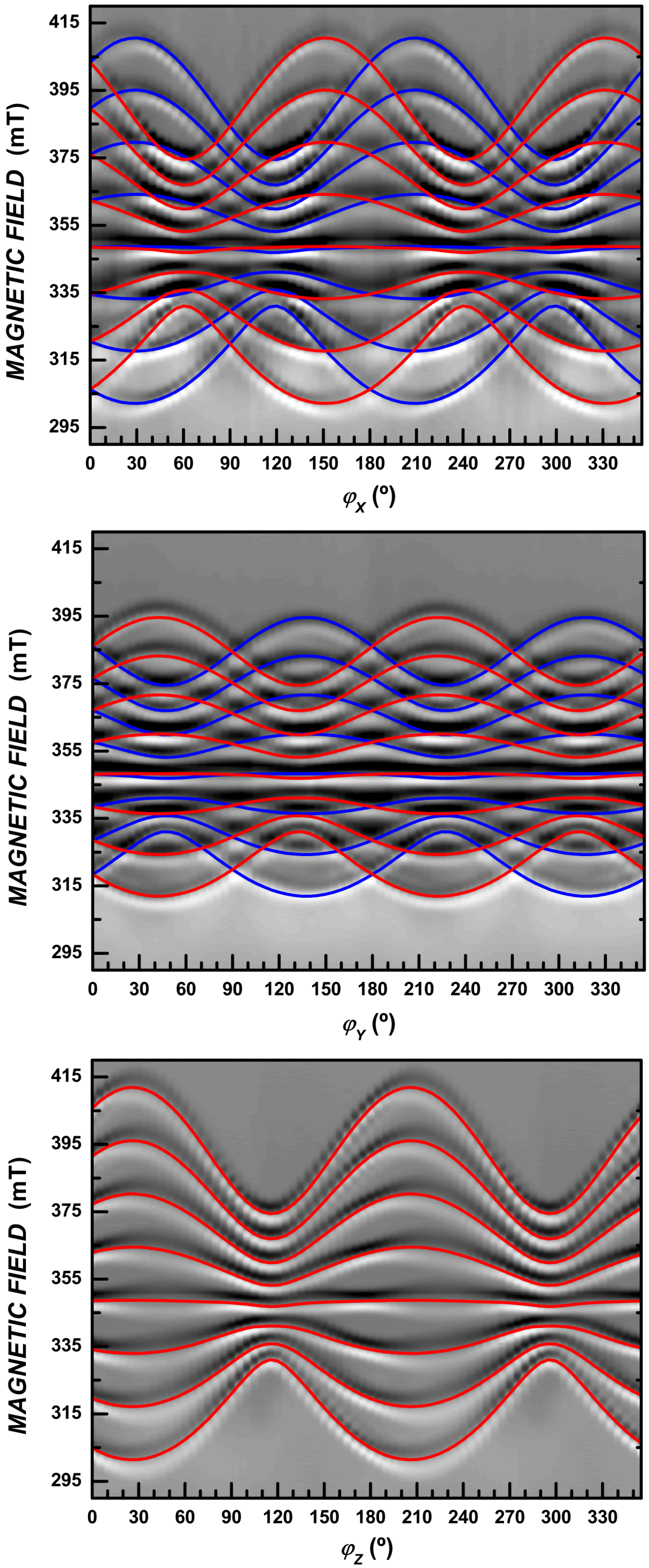

**Figure S8.** Full rotational diagrams for a single crystal of $\mathbf{1}^{\mathbf{VO}}$ at RT. Lines are the expected angle dependence calculated with the spin Hamiltonian. The contribution from the two magnetically inequivalent orientations of the molecules is represented in different colours (red and blue).

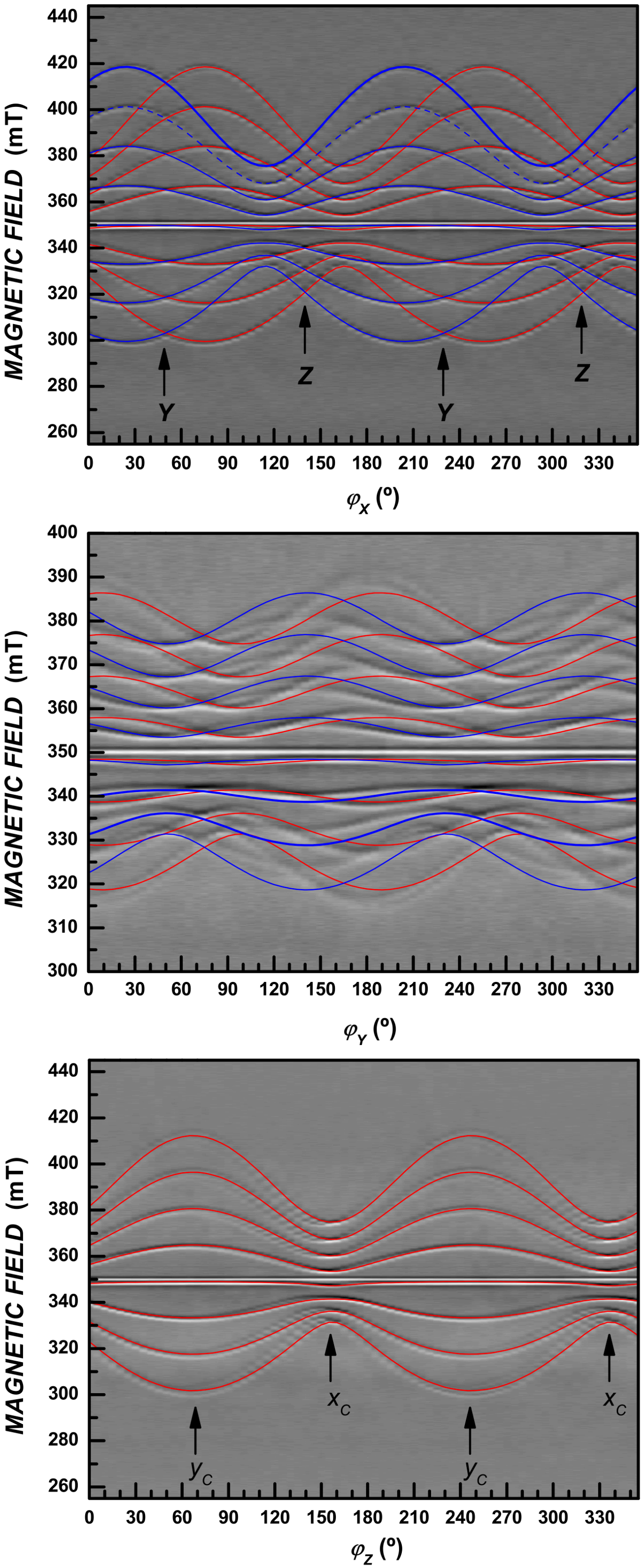

**Figure S9.** Full rotational diagrams for a single crystal of $\mathbf{1}^{VO}{}_{3\%}$ at RT. Lines are the expected angle dependence calculated with the spin Hamiltonian. The contribution from the two magnetically inequivalent orientations of the molecules is represented in different colours (red and blue). Arrows indicate the Y, Z, $x_C$ and $y_C$ axes as defined above. The isotropic signal at g = 2.01 present in all spectra is ascribed to a Ti(III) impurity.

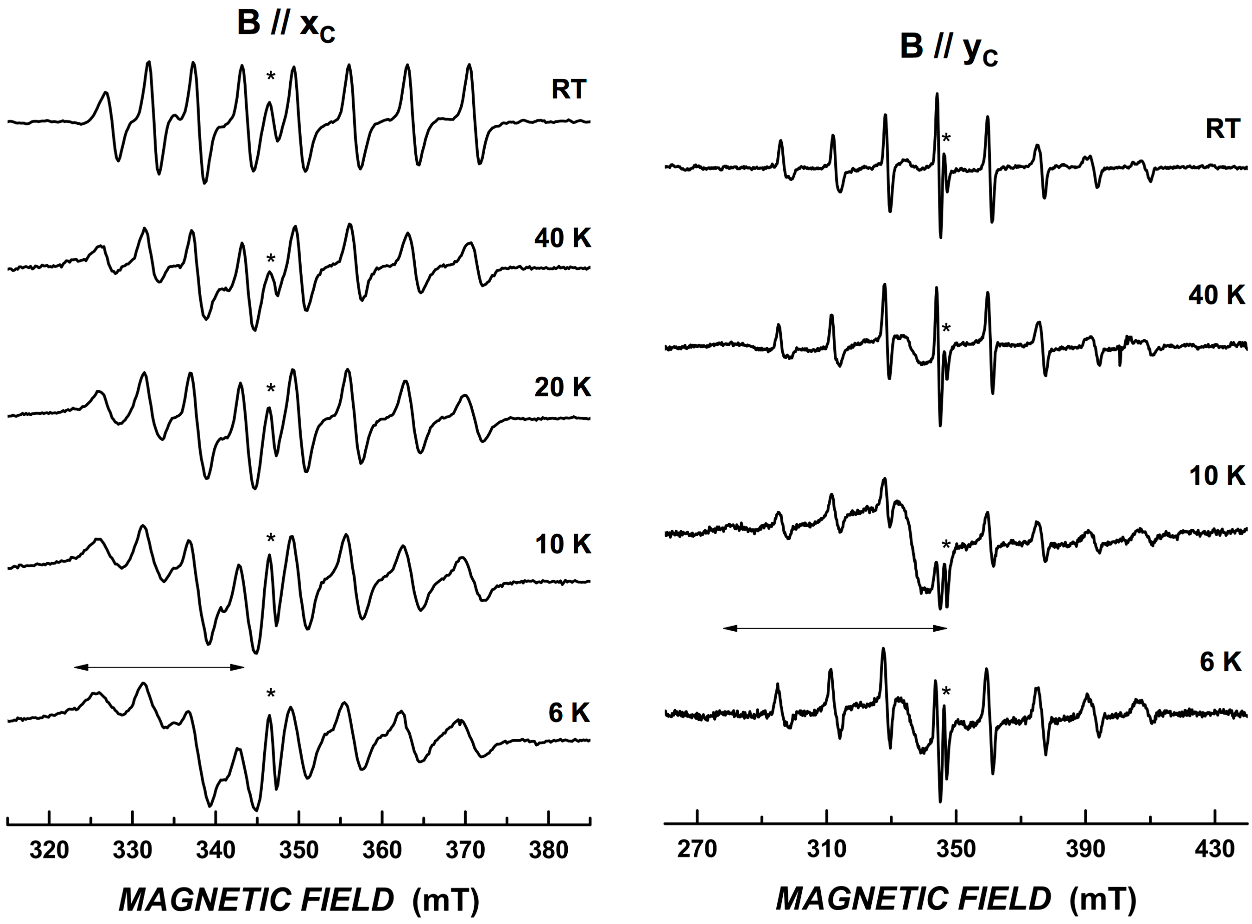

**Figure S10.** CW-EPR spectra of a single-crystal of $\mathbf{1}^{\mathrm{VO}}{}_{3\%}$ measured at different decreasing temperatures and for a magnetic field applied along the $x_C$ (left) and $y_C$ (right) crystal axes. A broad signal covering the 290-350 mT field range arises from Cu(II) ions on the surface of the cavity. The isotropic signal at g = 2.01 present in all spectra and indicated by a star is ascribed to a Ti(III) impurity. A broad signal arising from Cu(II) ions on the surface of the cavity is indicated by horizontal double arrows.

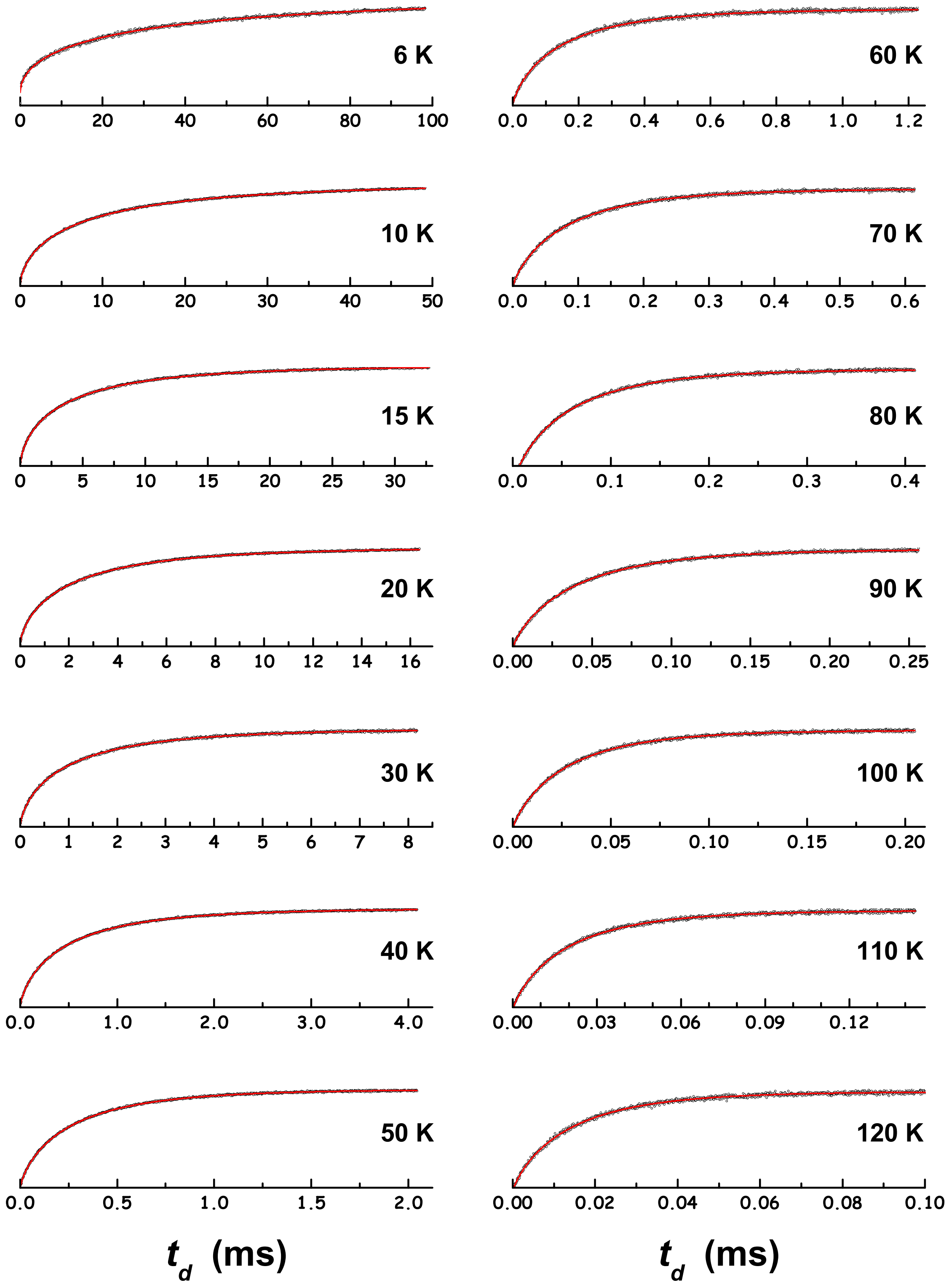

**Figure S11.** ESE detected Inversion Recovery ($\tau$ = 200 ns) as a function of delay time, $t_d$, for the frozen solution $\mathbf{1}^{\mathbf{VO}}_{\mathbf{sol}}$ at the indicated temperatures and $B$ = 346.6 mT (circles). Red lines correspond to a stretched exponential $t_d$ dependence modelled by:

$$y(t_d) = y_\infty - y_0 e^{-(t_d/\beta T_1)^\beta}$$

The derived values of $T_1$ are depicted in Figure 4 of the main article (see also Table S3).

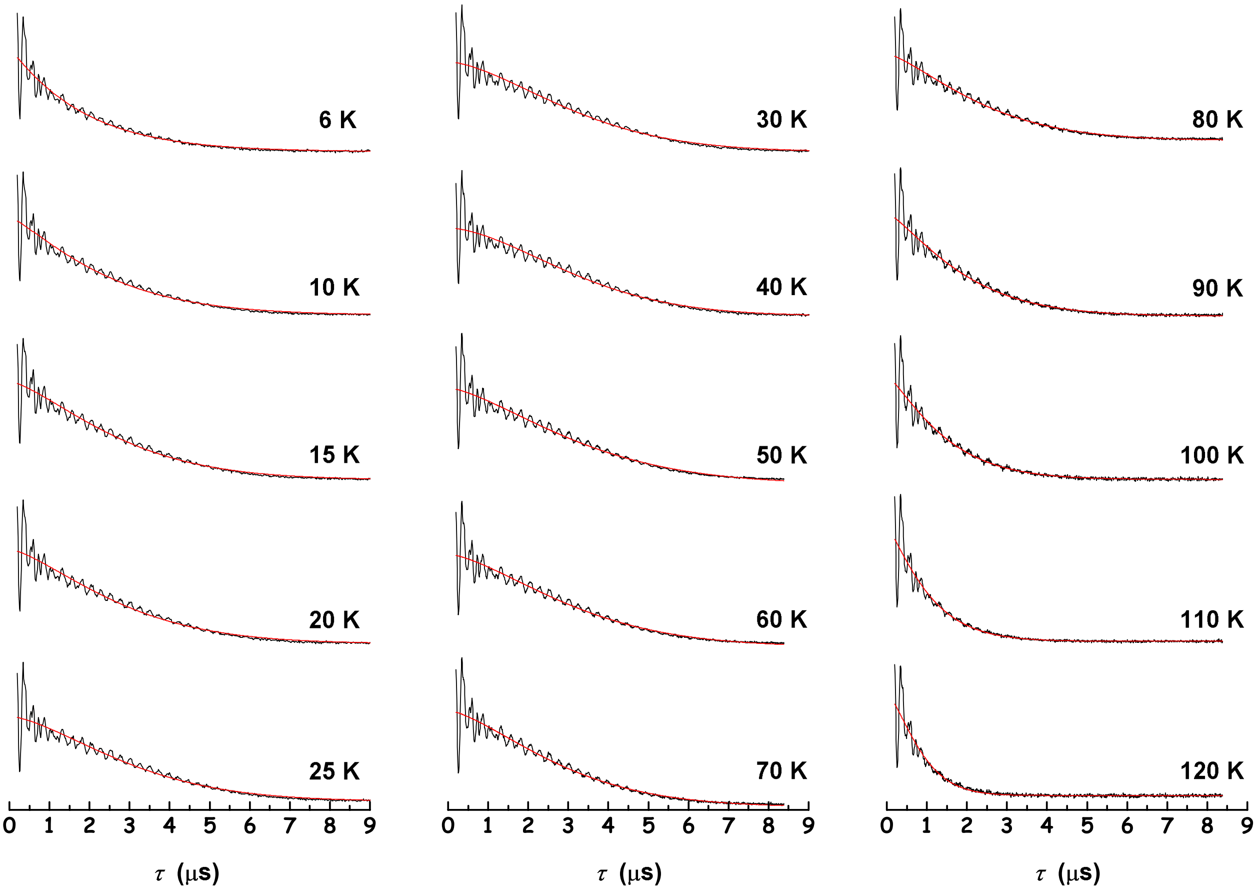

**Figure S12.** 2p ESE intensity as a function of inter-pulse interval, τ, measured on $\mathbf{1}^{\mathbf{VO}}_{\mathbf{sol}}$ at the indicated temperatures and *B* = 346.6 mT. Red lines are least-square fits with a stretched exponential:

$$y(\tau) = y_0 + A_{2p} e^{-\left(2\tau/T_2\ \right)^{\beta}}$$

The values of $T_2$ obtained from these fits are depicted in Figure 3 of the main text (see also Table S3).

At all temperatures, the derived values of $\beta$ are > 1 (in the range 1.05-1.70), which impedes to interpret it as a distribution of relaxation times. Values of $\beta$ > 1 have been associated with spin diffusion processes induced by either the dipolar interaction or the nucleus-nucleus interaction which modulates the spin dephasing through the hyperfine interaction. Lacking additional information, we prefer to avoid giving any interpretation. We trust the derived phase coherence times are robust, as no significant differences result from using the present stretched exponential model or a simple exponential with or without a low frequency modulation (see caption of Figure S13 below).

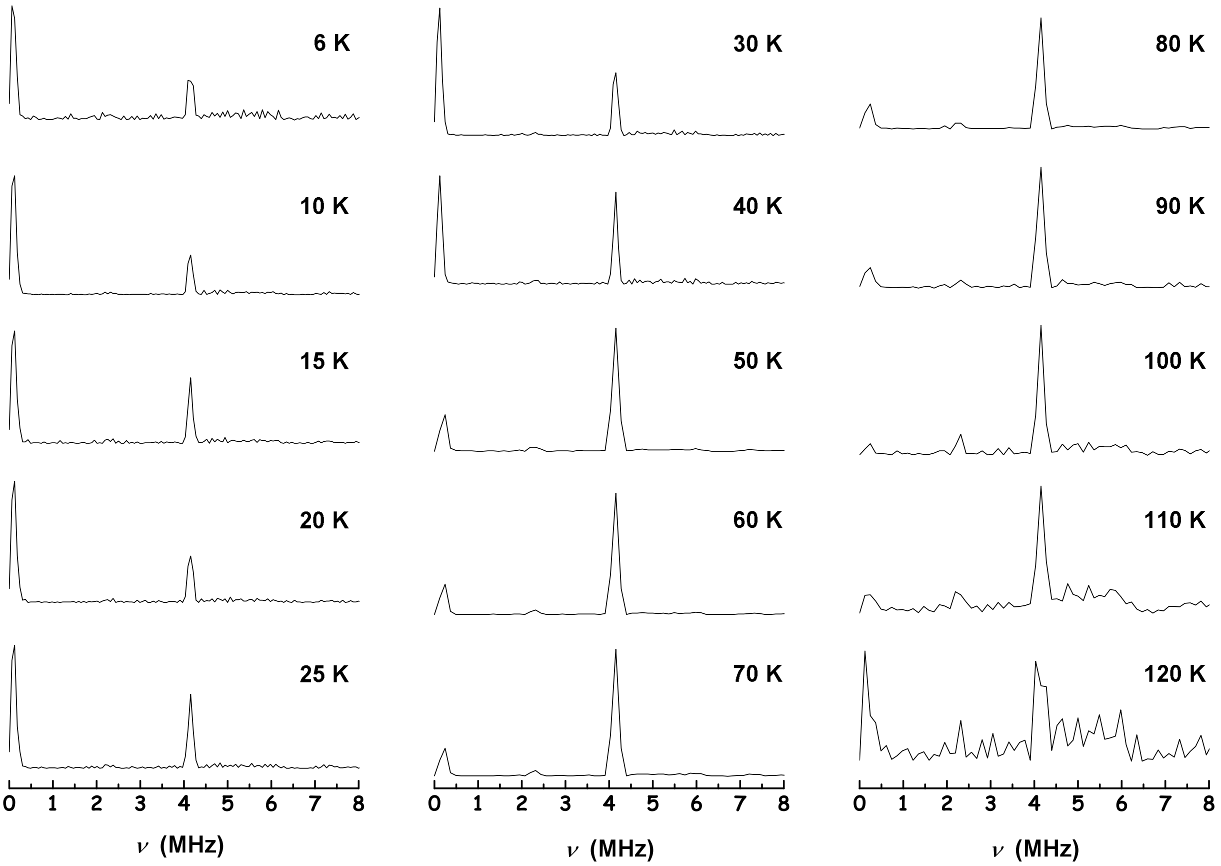

**Figure S13.** Power spectra of the modulation in the 2p ESE decay detected for $\mathbf{1^{VO}_{sol}}$ at the indicated temperatures and $B$ = 346.6 mT.

The observed low frequency contribution may be due to experimental variations of the background or small deviations from an exponential decay. It can be taken into account by considering an exponential decay with low frequency modulation using:

$$y(\tau) = y_0 + A\left\{e^{-2\tau/T_2} + ke^{-2\tau/T_D}\cos(2\pi\tau\nu) + \varphi_0\right\}$$

with the frequency $\nu$ in the range 0.10-0.14 MHz.

While the simulation of the 2p ESE decay is good and the low frequency contribution is then mostly removed from the resulting power spectra, the times $T_2$ and $T_D$ obtained in this way show significantly larger errors, especially at temperatures above 50 K. Since these are similar as those obtained with the stretched exponential model, we have preferred to keep the later.

**Table S3.** Parameters that provide the best fits to ESE detected Inversion Recovery signals and the 2p-ESE decay for $\mathbf{1}^{\mathbf{VO}}_{\mathbf{sol}}$ measured at 346.6 mT and variable temperature.

| $T$ (K) | $T_1$ (μs) | $\beta$ | $T_2$ (μs) | $\beta$ |
|---|---|---|---|---|
| 6 | 52573 ± 1521 | 0.534 ± 0.007 | 3.76 ± 0.20 | 1.05 ± 0.04 |
| 10 | 13050 ± 61 | 0.603 ± 0.003 | 5.17 ± 0.26 | 1.23 ± 0.04 |
| 15 | 5862 ± 19 | 0.639 ± 0.002 | 6.06 ± 0.28 | 1.41 ± 0.04 |
| 20 | 3168 ± 10 | 0.678 ± 0.002 | 6.16 ± 0.30 | 1.41 ± 0.04 |
| 25 | | | 6.82 ± 0.34 | 1.52 ± 0.04 |
| 30 | 1500 ± 6 | 0.679 ± 0.003 | 7.27 ± 0.36 | 1.60 ± 0.04 |
| 40 | 679 ± 2 | 0.720 ± 0.002 | 7.46 ± 0.36 | 1.70 ± 0.04 |
| 50 | 349 ± 1 | 0.752 ± 0.002 | 7.42 ± 0.69 | 1.46 ± 0.06 |
| 60 | 197.4 ± 1.2 | 0.766 ± 0.006 | 7.09 ± 0.61 | 1.50 ± 0.06 |
| 70 | 104.2 ± 0.5 | 0.805 ± 0.005 | 6.35 ± 0.50 | 1.46 ± 0.06 |
| 80 | 68.5 ± 0.3 | 0.803 ± 0.004 | 5.27 ± 0.38 | 1.38 ± 0.05 |
| 90 | 47.7 ± 0.2 | 0.825 ± 0.004 | 4.13 ± 0.28 | 1.28 ± 0.05 |
| 100 | 33.0 ± 0.2 | 0.841 ± 0.005 | 3.13 ± 0.21 | 1.23 ± 0.05 |
| 110 | 23.6 ± 0.1 | 0.829 ± 0.005 | 2.27 ± 0.16 | 1.21 ± 0.06 |
| 120 | 16.7 ± 0.1 | 0.829 ± 0.007 | 1.92 ± 0.15 | 1.41 ± 0.07 |

**Table S4.** Relaxation times $T_1$ and $T_2$ for relevant vanadyl-based compounds derived from pulsed-EPR studies on frozen solutions.

| Compound | $T_1$ (ms) @ 10 K$^b$ | max. $T_2$ (μs) | concentration | solvent | *Ref.* |
|---|---|---|---|---|---|
| VOTCPPEt | 130 | 7.5 @ 40 K | 0.46 mM | $CDCl_3$/tol | this work |
| $VO(dpm)_2$ | 0.85 | 2.7 @ 20 K | 1 mM | $CD_2Cl_2$/tol-d$^8$ | [9] |
| $[VO(napthcat)_2]^{2-}$ | 6 | 6.5 @ 25 K | 1 mM | $CH_2Cl_2/C_6H_6$ | [10] |
| VOPc$^a$ | 204 / 20$^b$ | 24 @ 10 K | 0.5 mM | $D_2SO_4$ | [11] |
| $[VO(C_8S_8)_2]^{2-}$ | 187 / 80$^b$ | 3.5 @ 10 K | 0.5 mM | dmf-d$^7$/tol-d$^8$ | [12] |
| $[VO(C_3H_6S_2)_2]^{2-}$ | 17.5 | 10.3 @ 20 K | 0.1 mM | dmf-d$^7$/tol-d$^8$ | [13] |

a: using Q band, while the rest of studies uses X-band; b: in cases where the experimental data has been fitted with a bi-exponential model, both slow and fast relaxation times are given.

---

[9] L. Tesi, E. Lucaccini, I. Cimatti, M. Perfetti, M. Mannini, M. Atzori, E. Morra, M. Chiesa, A. Canschi, L. Sorace, R. Sessoli, Chem. Sci., 2016, 7, 2074

[10] M. Atzori, S. Benci, E. Morra, L. Tesi, M. Chiesa, R. Torre, L. Sorace, R. Sessoli, Inorg. Chem., 2018, 57, 731

[11] K. Bader, M. Winkler, J. van Slageren, Chem. Commun., 2016, 52, 3623

[12] C-J. Yu, M. J. Graham, J. M. Zadrozny, J. Niklas, M. D. Krzyaniak, M. R. Wasielewski, O. G. Poluetkov, D. E. Freedman, J. Am. Chem. Soc., 2016, 138, 14678

[13] M. J. Graham, C-J. Yu, M. D. Krzyaniak, M. R. Wasielewski, D. E Freedman, J. Am. Chem. Soc., 2017, 139, 3196

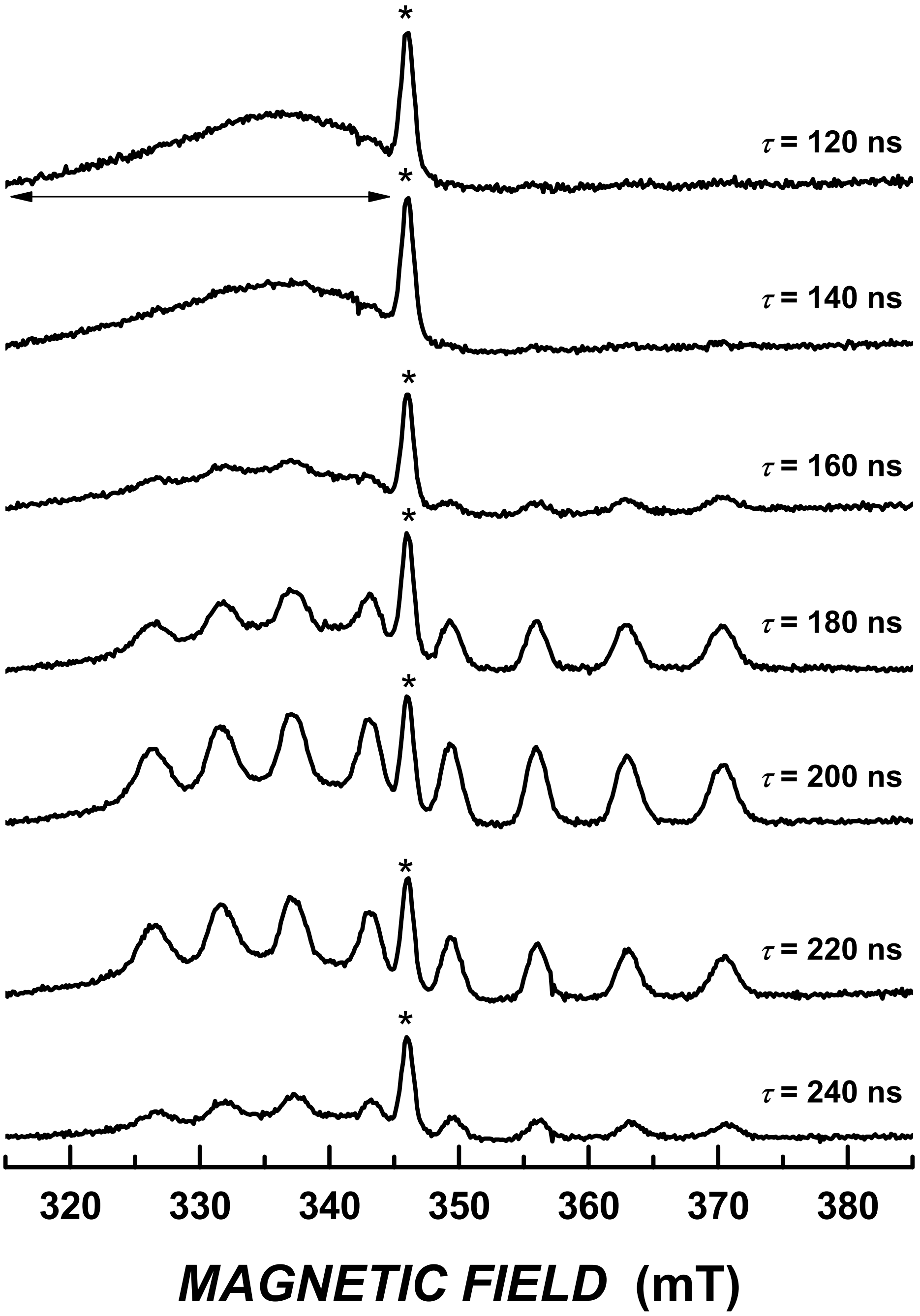

**Figure S14.** ESE-detected EPR spectra measured on a single-crystal of $\mathbf{1}^{\mathrm{VO}}{}_{3\%}$ at 6 K and for variable $\tau$, with the magnetic field applied along the $x_C$ crystal axis. A broad signal covering the 290-350 mT field range is detected at all $\tau$ arising from Cu(II) ions on the surface of the cavity. The isotropic signal at g = 2.01 present in all spectra and marked with a star is ascribed to a Ti(III) impurity.

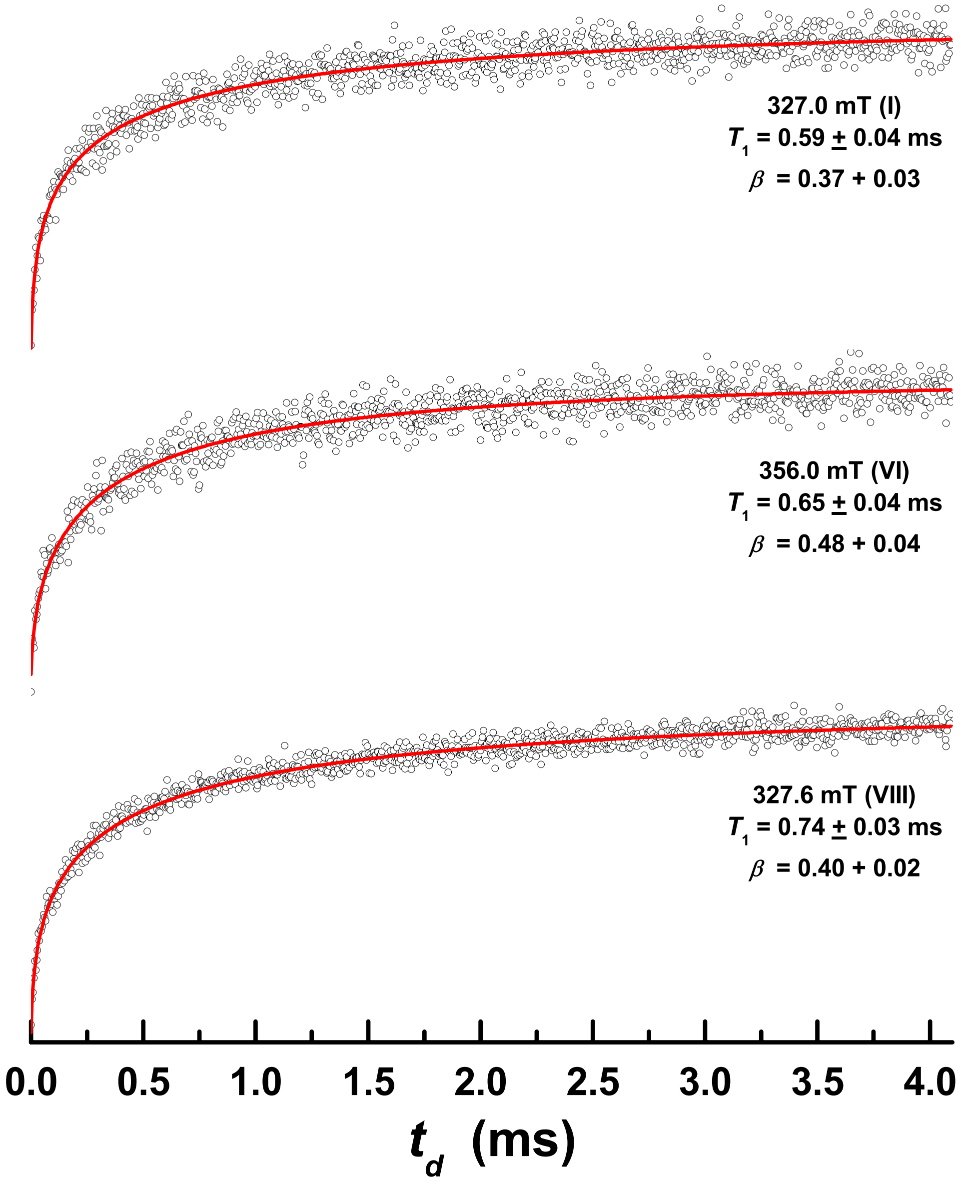

**Figure S15.** ESE detected Inversion Recovery ($\tau$ = 200 ns) measured as a function of delay time, $t_d$, on $\mathbf{1}^{\mathbf{VO}}{}_{\mathbf{3\%}}$ at 6 K and for the indicated magnetic fields applied along the $x_C$ direction (circles). Red lines correspond to a stretched exponential $t_d$ dependence modelled by:

$$y(t_d) = y_\infty - y_0 e^{-\left(t_d/\beta T_1\right)^\beta}$$

and the indicated best-fit parameters $T_1$ and $\beta$. $T_1$ values are depicted plotted in Figure 5 of the main article.

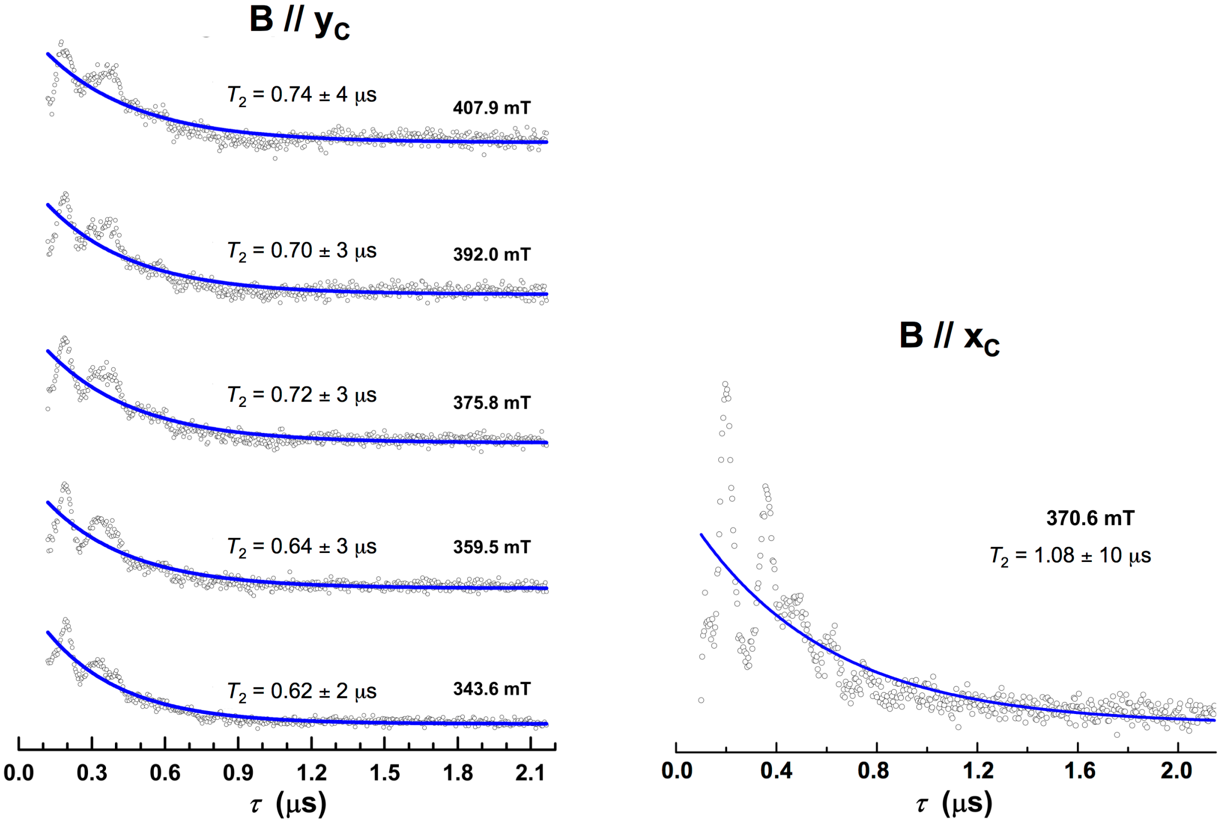

**Figure S16.** 2p ESE intensity measured as a function of inter-pulse interval, τ, on $\mathbf{1}^{\mathbf{VO}}_{\mathbf{3\%}}$ at 6 K and for the indicated magnetic field orientations and values (circles). Blue lines are least-squares fits with an exponential decay:

$$y(\tau) = y_0 + A_{2p} e^{-2\tau/T_2}$$

and the indicated values of $T_2$, which are depicted in Figure 4 of the main text.

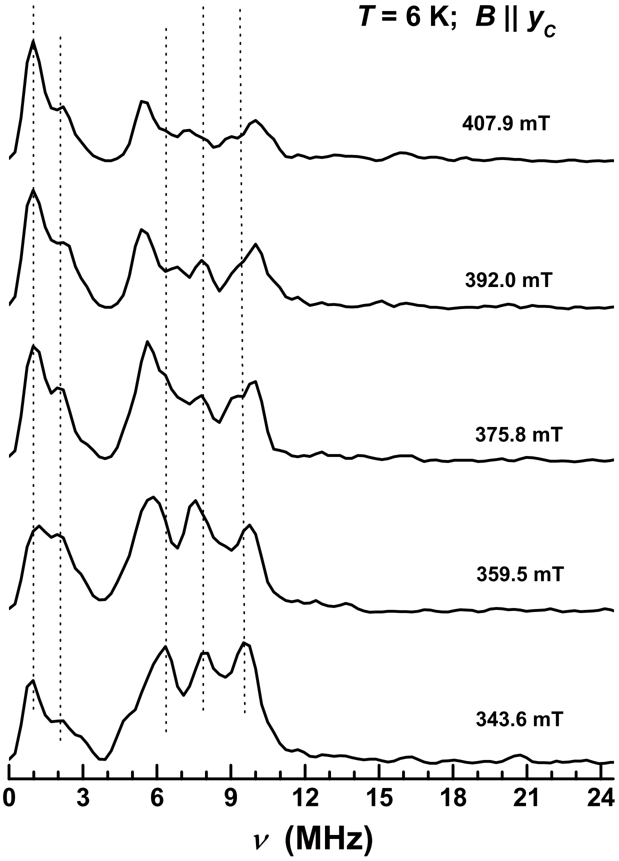

**Figure S17.** Power spectra of the modulation in the 2p ESE decay detected for $\mathbf{1}^{\mathrm{VO}}{}_{3\%}$ at $T$ = 6 K and the indicated magnetic fields applied parallel to the $y_{\mathrm{C}}$ axis. Vertical dash lines are guides to the eye indicating the position of the main frequencies of modulation at the lowest field.

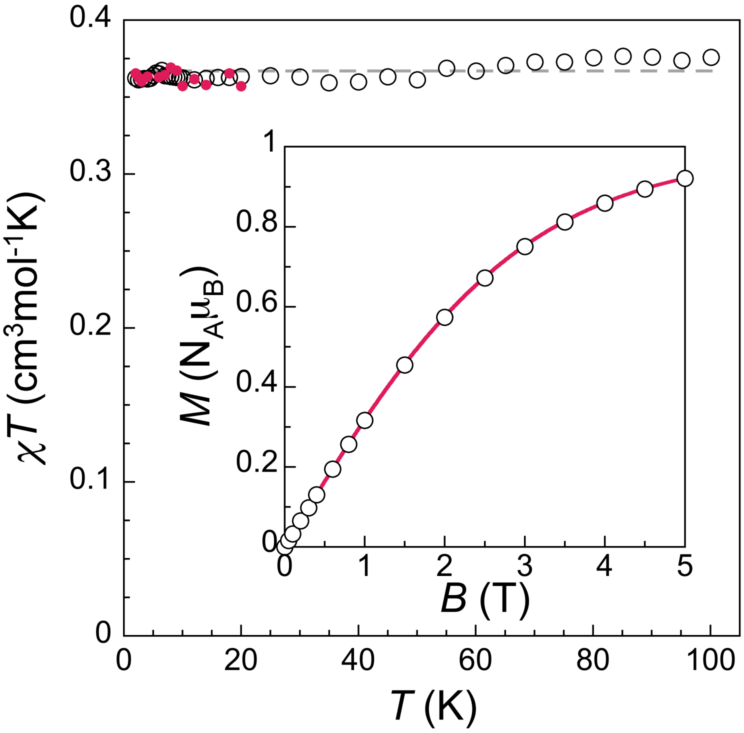

**Figure S18.** Temperature dependence of the $\chi T$ product of $\mathbf{1}^{\mathbf{VO}}$ derived from magnetization measurements at 0.01 T (open symbols) and from zero-field *ac* susceptibility measurements at 10 Hz (solid red symbols). The dashed grey line represents the Curie law for $C$ = 0.367 cm$^3$mol$^{-1}$. Inset: magnetization isotherm of $\mathbf{1}^{\mathbf{VO}}$ measured at $T$ = 2 K with the corresponding Brillouin function for $S$ = 1/2 and g = 1.98 shown as a red solid line. Both sets of data are thus in excellent agreement with the EPR data from which $g_{\parallel}$ = 1.963 and $g_{\perp}$ = 1.99 were derived.

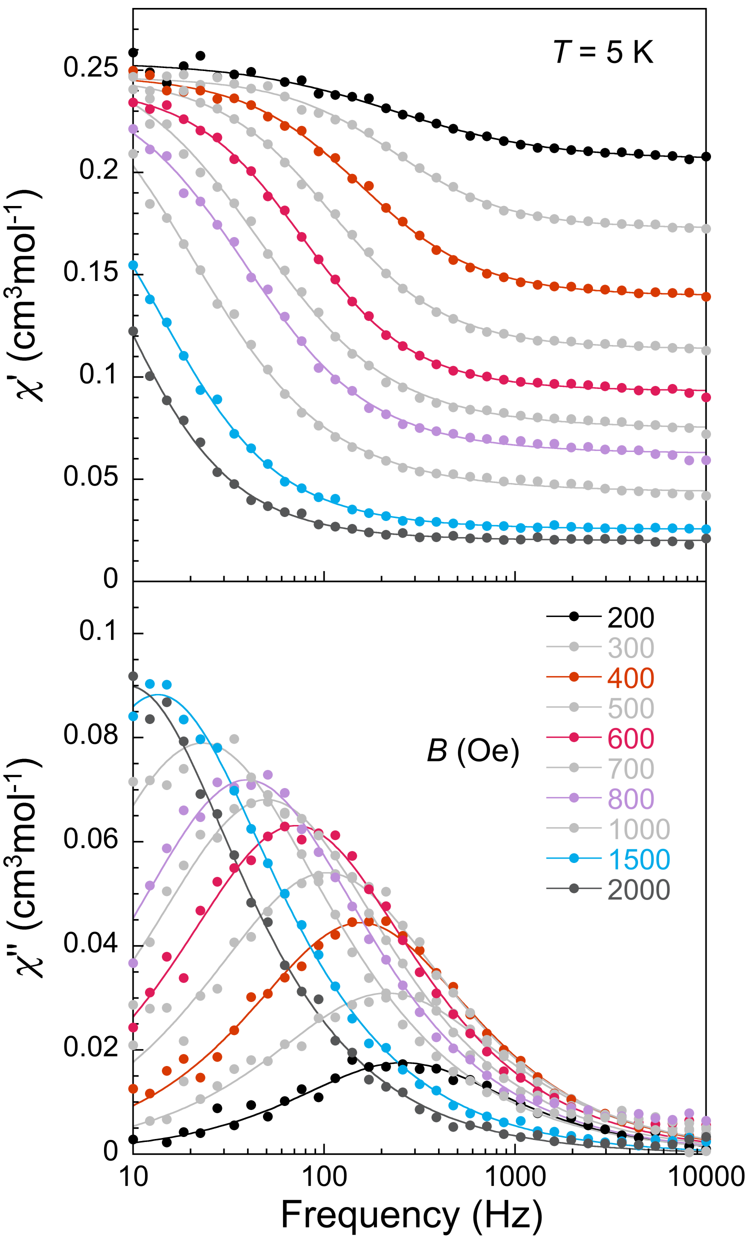

**Figure S19.** Frequency dependence of the in-phase (top) and out-of-phase (bottom) *ac* magnetic susceptibility components of $\mathbf{1}^{\mathbf{VO}}$ measured at 5 K and for different *dc* applied magnetic fields, as indicated. Lines are least-square fits to the Cole-Cole expressions for $\chi'$ and $\chi''$ that allow determining the characteristic spin relaxation time $\tau$:

$$\chi'(\omega) = \chi_S + (\chi_T - \chi_S)\frac{1 + (\omega\tau)^{\beta}\cos\left(\frac{\pi\beta}{2}\right)}{1 + 2(\omega\tau)^{\beta}\cos\left(\frac{\pi\beta}{2}\right) + (\omega\tau)^{2\beta}}$$

$$\chi''(\omega) = (\chi_T - \chi_S)\frac{(\omega\tau)^{\beta}\sin\left(\frac{\pi\beta}{2}\right)}{1 + 2(\omega\tau)^{\beta}\cos\left(\frac{\pi\beta}{2}\right) + (\omega\tau)^{2\beta}}$$

in which $\omega$ is the angular frequency, $\chi_T$ the isothermal susceptibility, $\chi_S$ the adiabatic susceptibility and $\beta$ describes a limited distribution of relaxation times (0.8-0.9 range). For a $S = 1/2$ spin system, $\tau$ coincides with the spin-lattice relaxation time $T_1$.

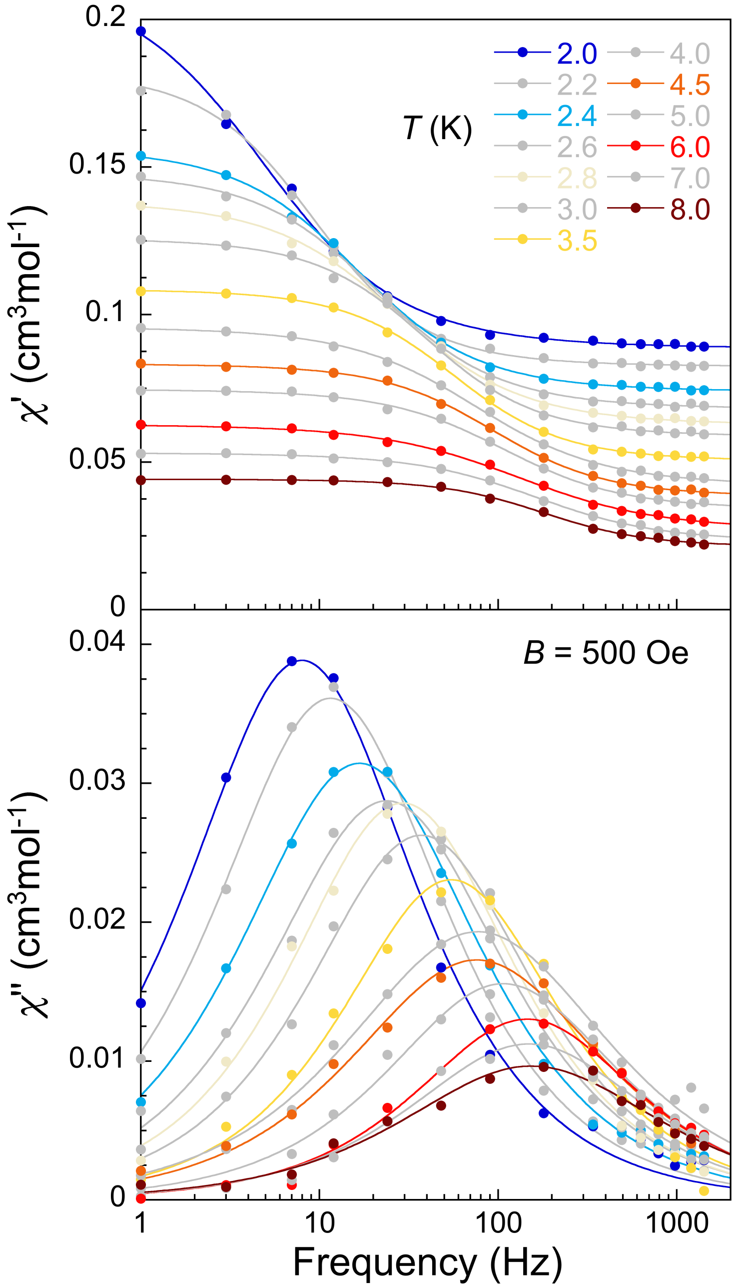

**Figure S20.** Frequency dependence of the in-phase (top) and out-of-phase (bottom) *ac* magnetic susceptibility components of $\mathbf{1}^{\mathbf{VO}}$ measured at 500 Oe and for variable *T*, as indicated. Lines are least-square fits to the Cole-Cole expressions for $\chi'$ and $\chi''$ (see Fig S18). Data obtained with a commercial magnetometer using a SQUID sensor.

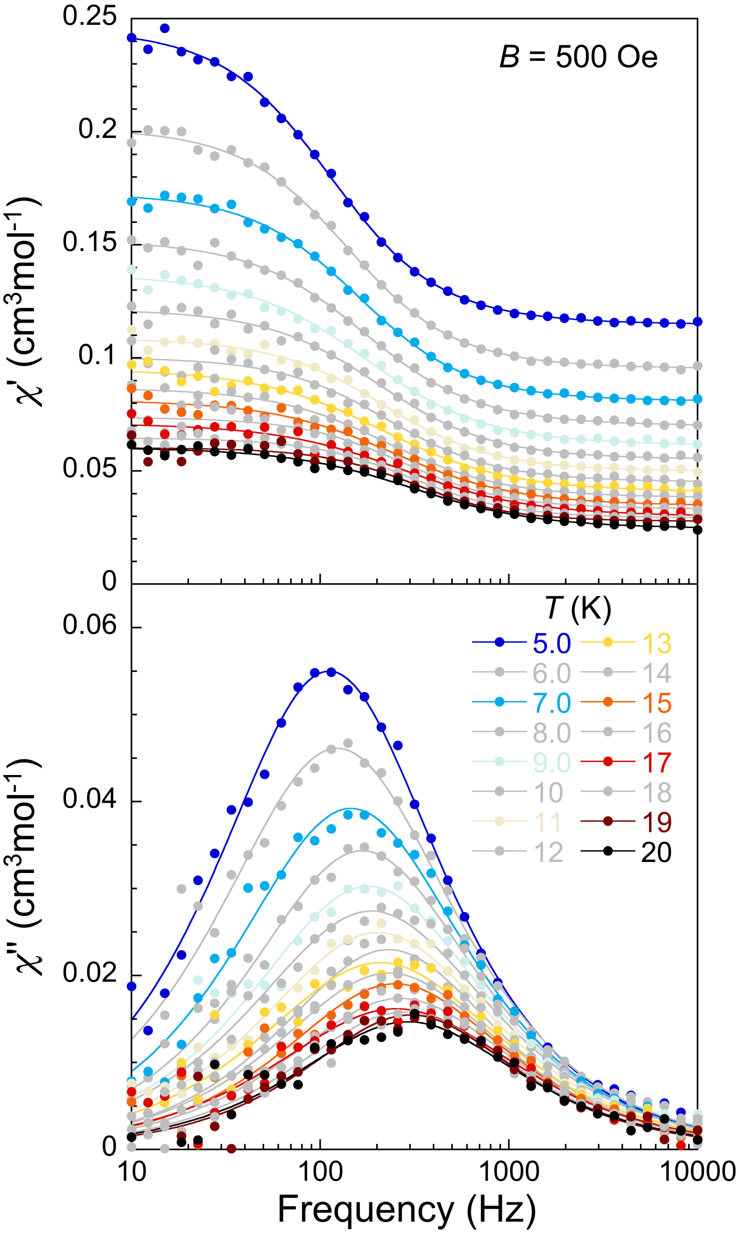

**Figure S21.** Frequency dependence of the in-phase (top) and out-of-phase (bottom) *ac* magnetic susceptibility components of $\mathbf{1}^{\mathbf{VO}}$ measured at 500 Oe and for variable *T*, as indicated. Lines are least-square fits to the Cole-Cole expressions for $\chi$' and $\chi$" (see Fig S18). Data obtained with the ACMS option of a commercial PPMS set-up.

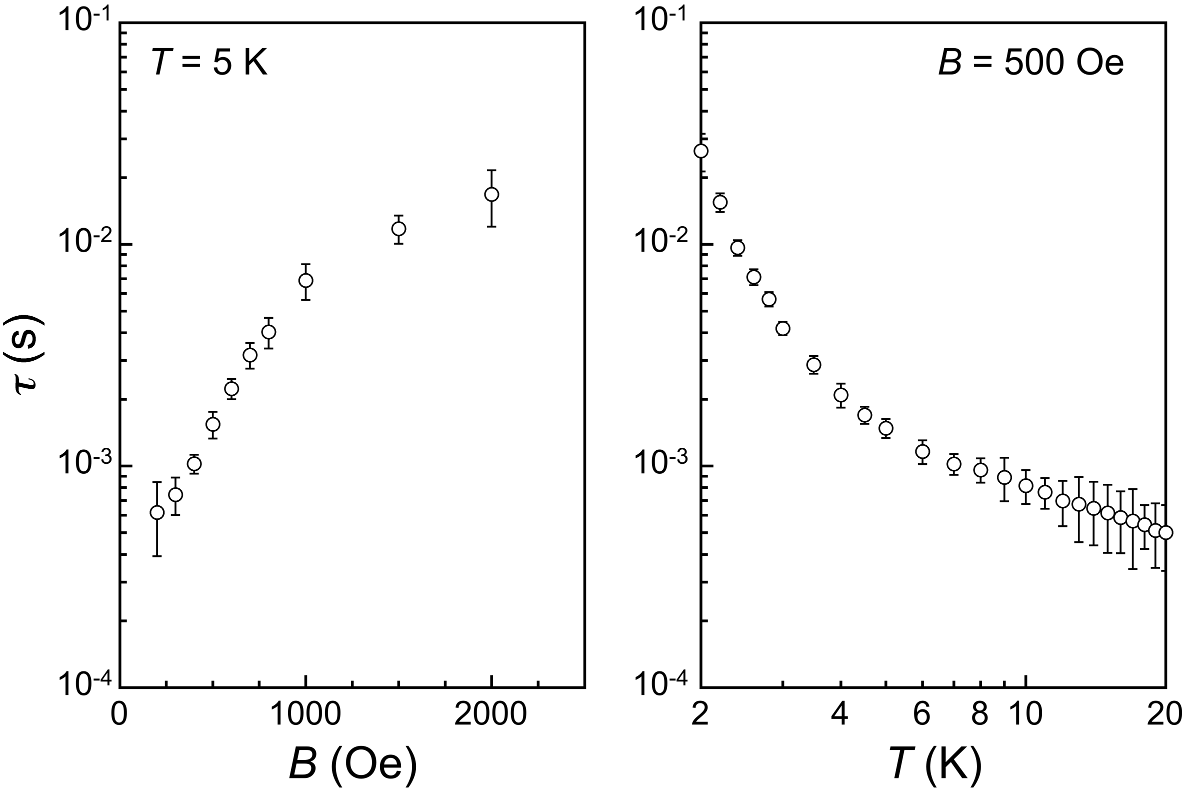

**Figure S22.** Spin-lattice relaxation time of $\mathbf{1}^{\mathbf{VO}}$ determined from the fit of ac magnetic susceptibility data (Figs. S18-S20).

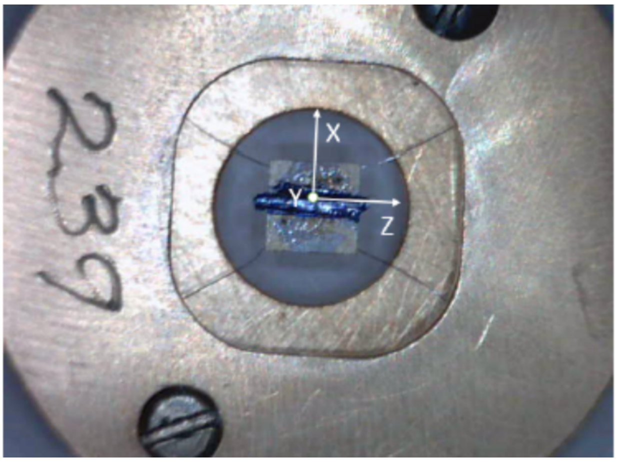

**Figure S23.** Image of a calorimeter platform hosting a single crystal of $\mathbf{1}^{\mathbf{VO}}$. The arrows show the laboratory frame. The magnetic field was applied along Z.

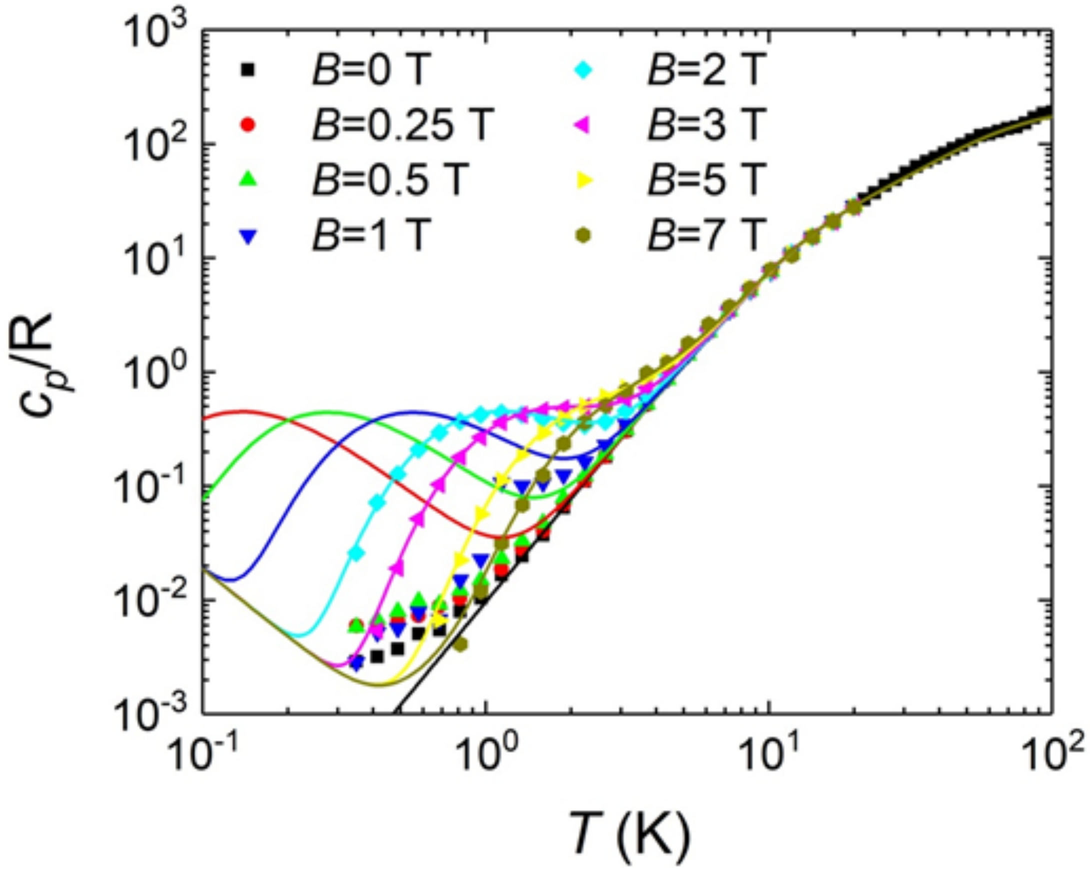

**Figure S24.** Heat capacity of a single crystal of $\mathbf{1}^{\mathbf{VO}}$ measured under different magnetic fields. Lines are simulations based on the parameters of the spin Hamiltonian derived from EPR measurements (see Fig. 2 of main text).

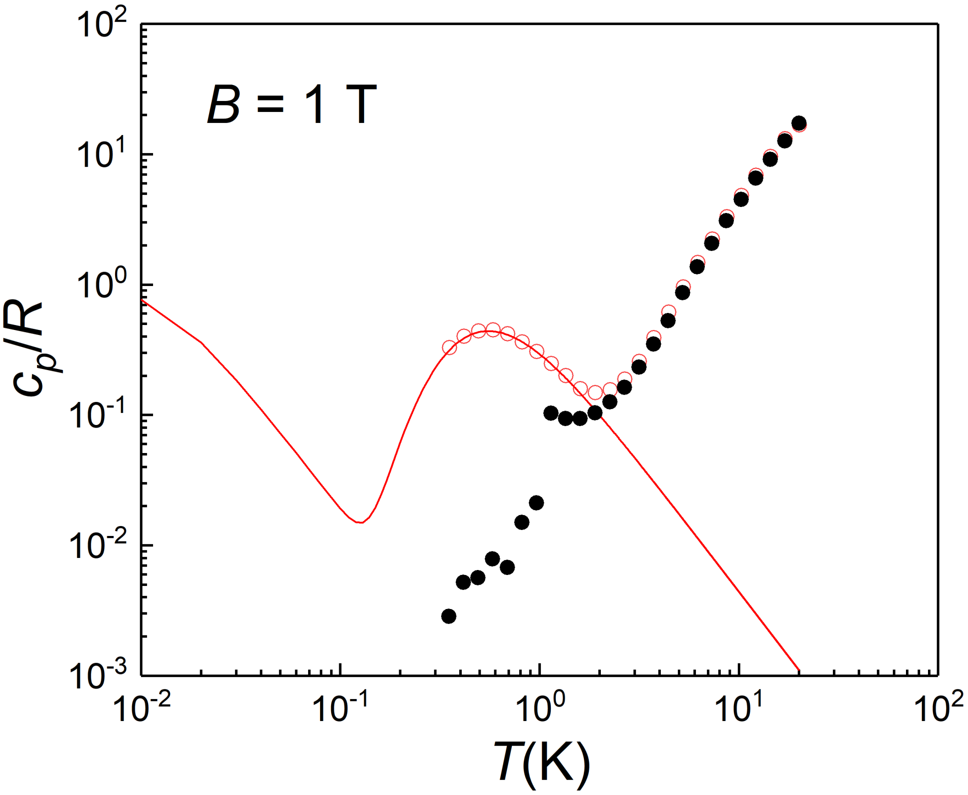

**Figure S25.** Specific heat of **1**$^{\mathbf{VO}}$ measured at $B$ = 1 T and for two different experimental times. At $T$ = 0.96 K, the experimental time was 0.11 s for the solid dots and 4.4 s for the open symbols. In the former case, the spins are unable to attain equilibrium with the crystal lattice and the specific heat cannot reach its thermal equilibrium value, shown by the red solid line.

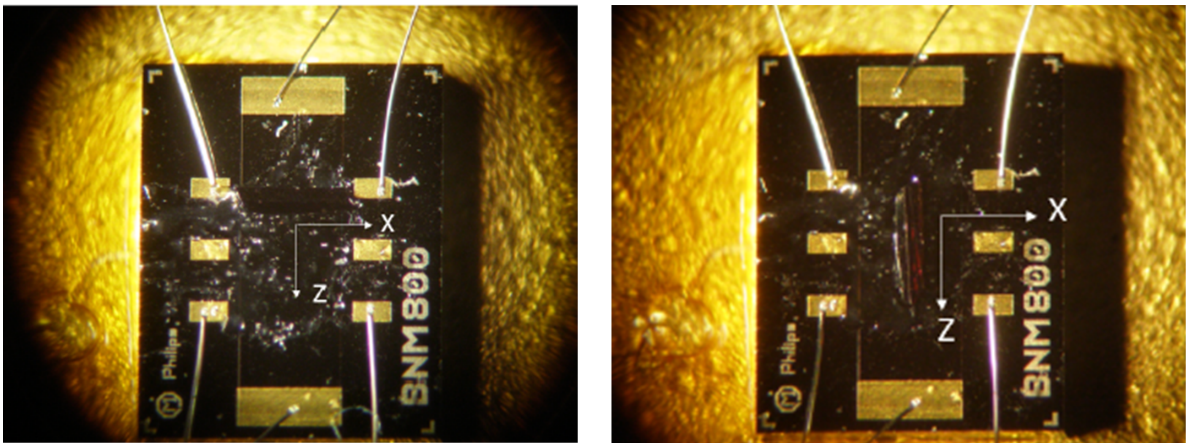

**Figure S26.** Pictures of a micro-Hall magnetometer hosting a single crystal of $\mathbf{1}^{\mathrm{VO}}$ in two different orientations. The magnetic field was applied along the Z laboratory axis.

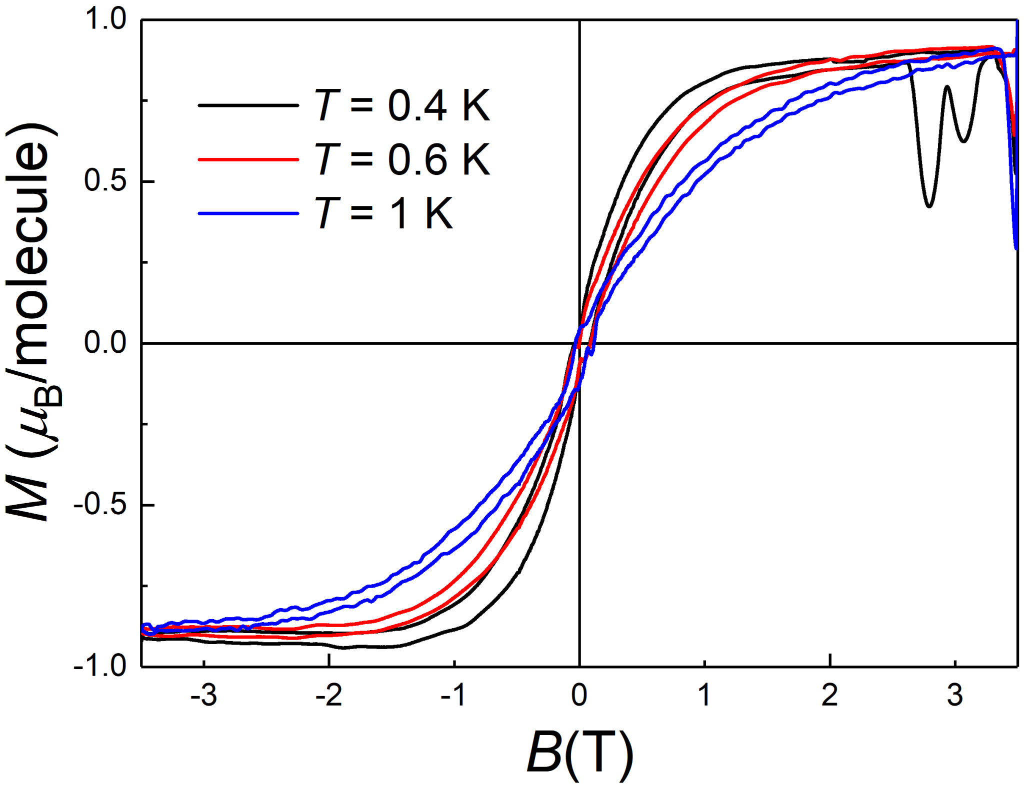

**Figure S27.** Magnetization hysteresis loops of a single crystal of $\mathbf{1}^{\mathrm{VO}}$ measured with its long axis oriented along the X laboratory axis at different temperatures (left panel of Figure S26). The magnetic field sweeping rate was 1 T/min.

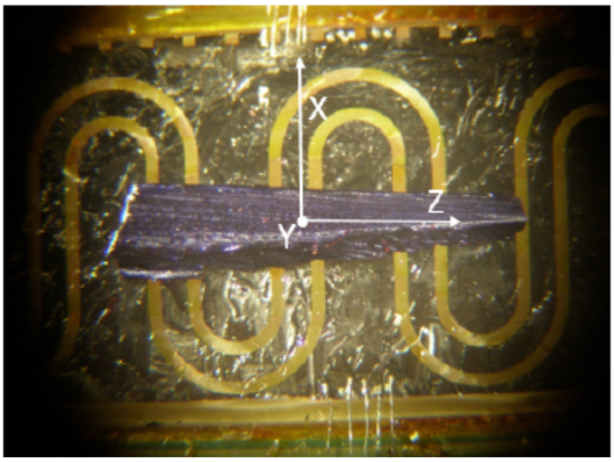

**Figure S28.** Picture of a Nb superconducting transmission line hosting a single crystal of $\mathbf{1}^{\mathbf{VO}}$. The magnetic field was applied along the X, Y and Z laboratory axis.

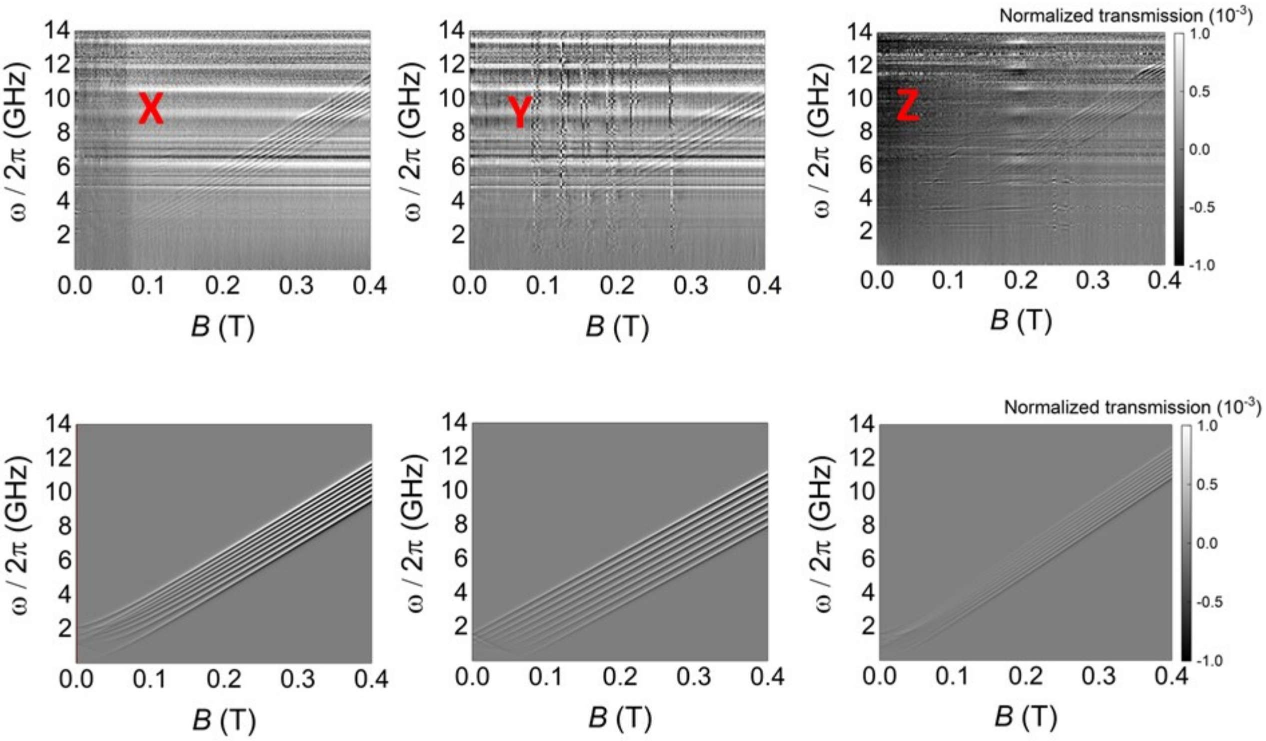

**Figure S29.** Grey scale two-dimensional plots of the normalized transmission through a superconducting transmission line coupled to a single crystal of $\mathbf{1}^{\mathbf{VO}}$ measured versus frequency $\omega$ and magnetic field applied along the laboratory axes X (left), Y (center) and Z (right). Top panels show experimental data and bottom panels show numerical simulations based on the spin Hamiltonian (Eq. (1) of the main text).

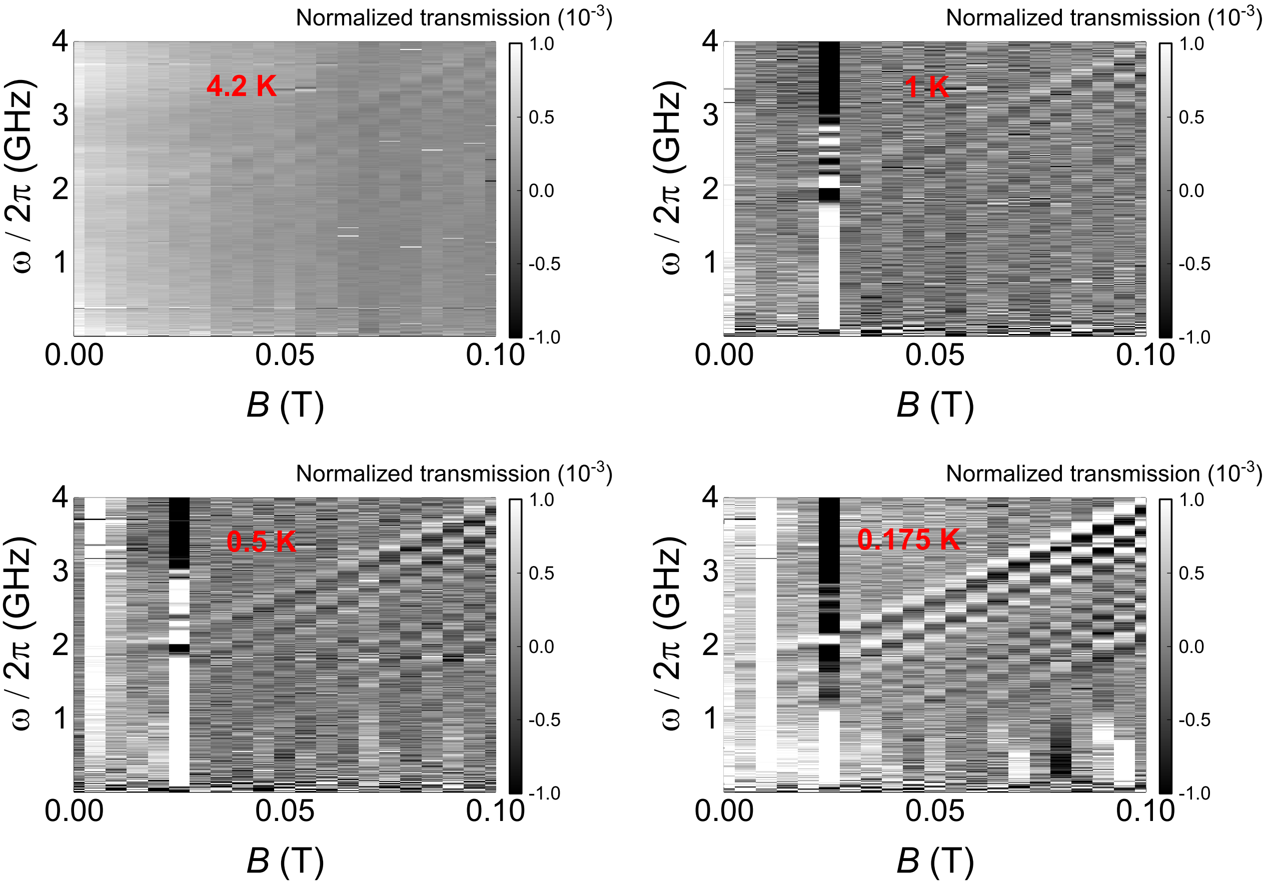

**Figure S30.** Low fields 2D plots of the normalized transmission through a superconducting transmission line coupled to a single crystal of $\mathbf{1^{VO}}$ measured versus frequency $\omega$ at decreasing temperatures as indicated. The magnetic field was applied along the Z laboratory axis.

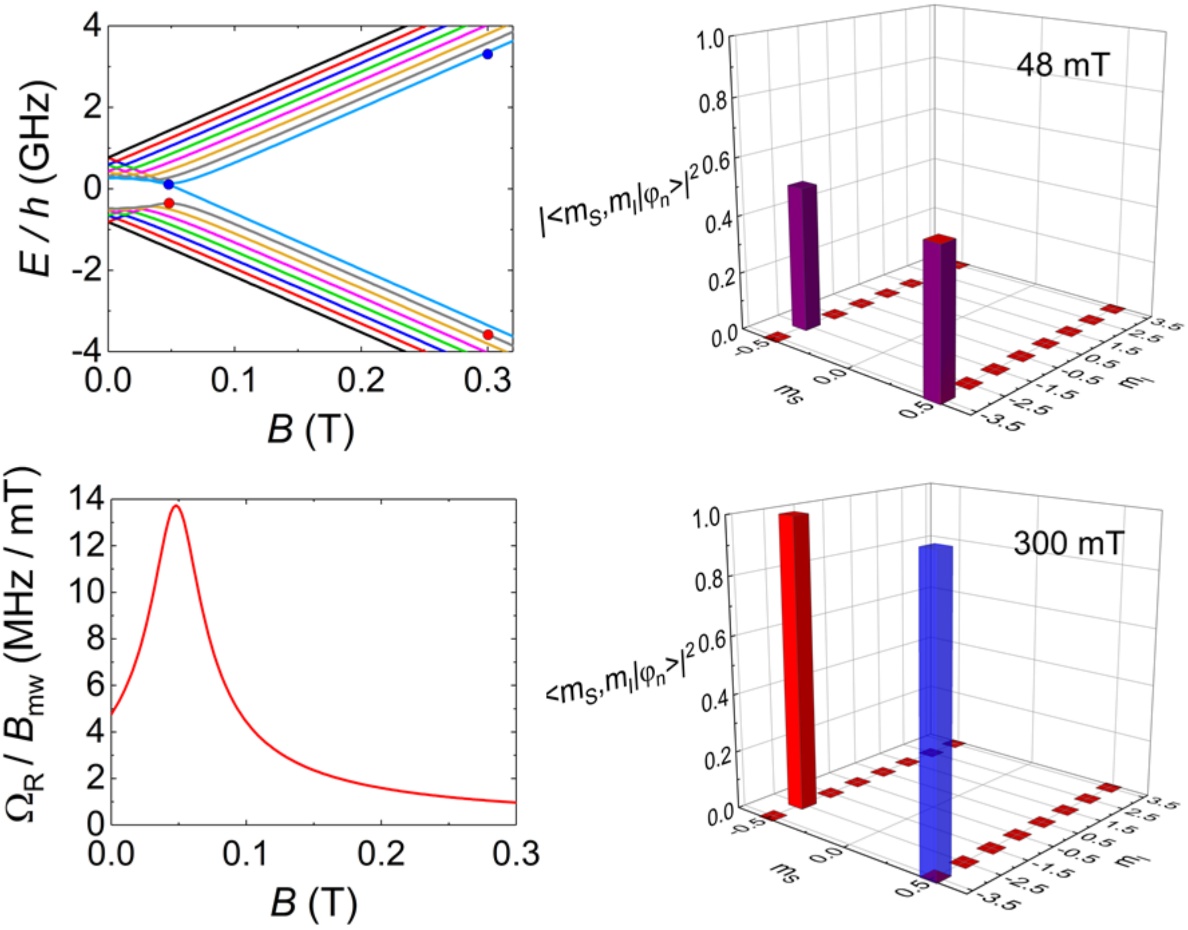

**Figure S31.** Link between electronuclear entanglement and universality for a simple situation where the magnetic field *B* is applied along the molecular anisotropy axis *z*. Left, top: energy level scheme. The red and blue dots show the energies of levels 7 and 9 at *B* = 0.05 T and 0.3 T. Left, bottom: Rabi frequency between the energy eigenstates associated with these levels, which shows a maximum near the level anticrossing. Right: Wave functions of these levels at 0.048 T and 0.3 T. They become maximally entangled near the anticrossing (thus leading to maximum $\Omega_R$) and factorize as a product of nuclear and electronic spin states at high field.

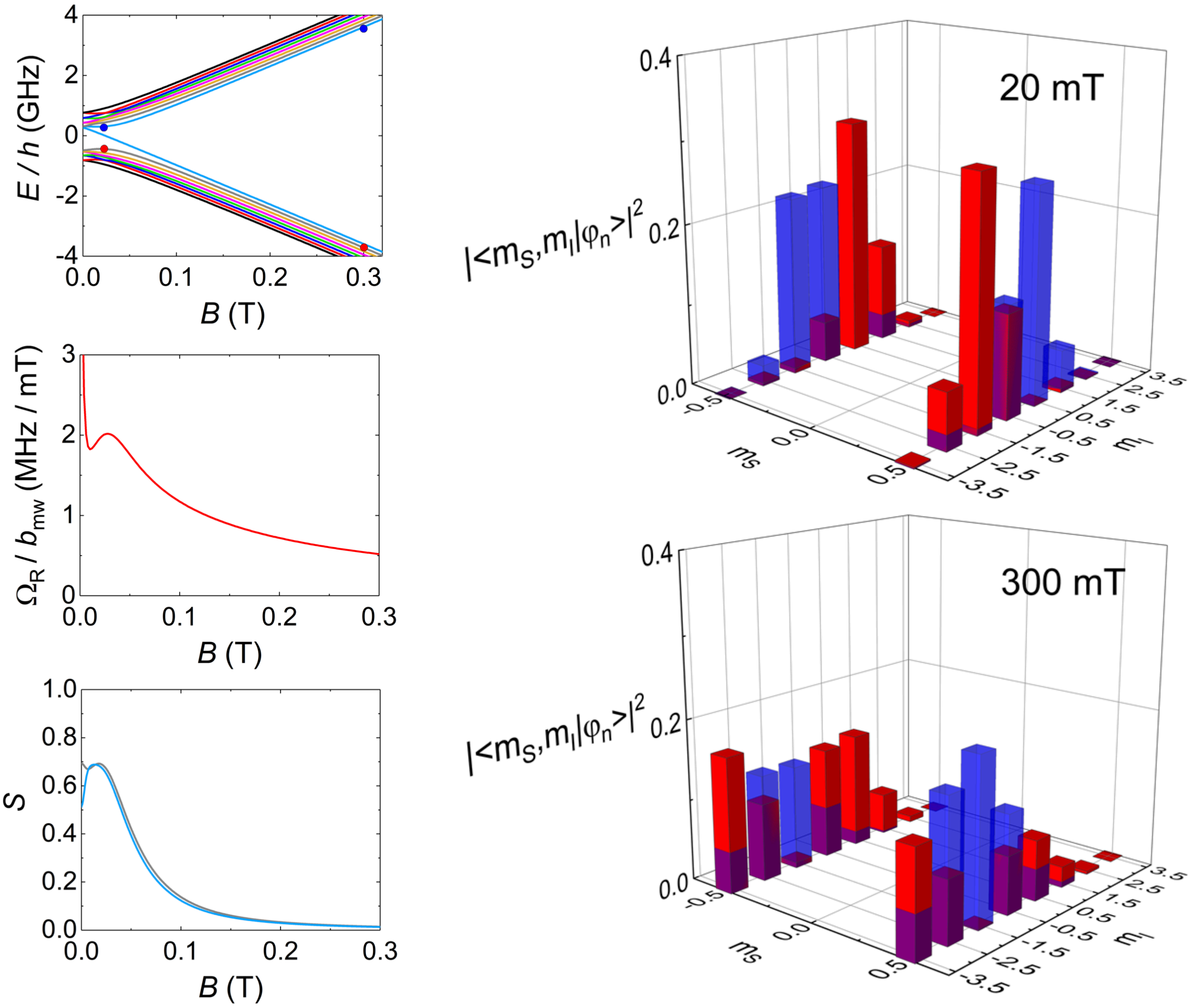

**Figure S32.** Link between electronuclear entanglement and universality for a magnetic field applied along the laboratory *X* axis (Fig. S28). In this case, the wave functions become more complex even for separable states. Therefore, we introduce information about the entanglement entropy *S* (or von Neumann entropy) $S = -Tr[\rho_I ln \rho_I]$, where $\rho_I = Tr_S \rho$ is a reduced density matrix and $\rho = |\varphi\rangle\langle\varphi|$ is the density matrix that describes any electronuclear spin eigenstate $|\varphi\rangle$. This entropy vanishes for separable states and approaches 1 when the electronic and nuclear spins are maximally entangled. Left, top: energy level scheme. The red and blue dots show the energies of levels 7 and 9 at *B* = 0.02 T and 0.3 T. Left, center: Rabi frequency between the energy eigenstates associated with these levels, which shows a maximum near the level anticrossing. Left, bottom: entanglement entropy. Right: Wave functions of these levels at 0.02 T and 0.3 T. They become maximally entangled near the anticrossing (thus leading to maximum $\Omega_R$) and factorize as a product of nuclear and electronic spin states at high field, but remain in both cases superpositions of different electronic and nuclear spin projections.

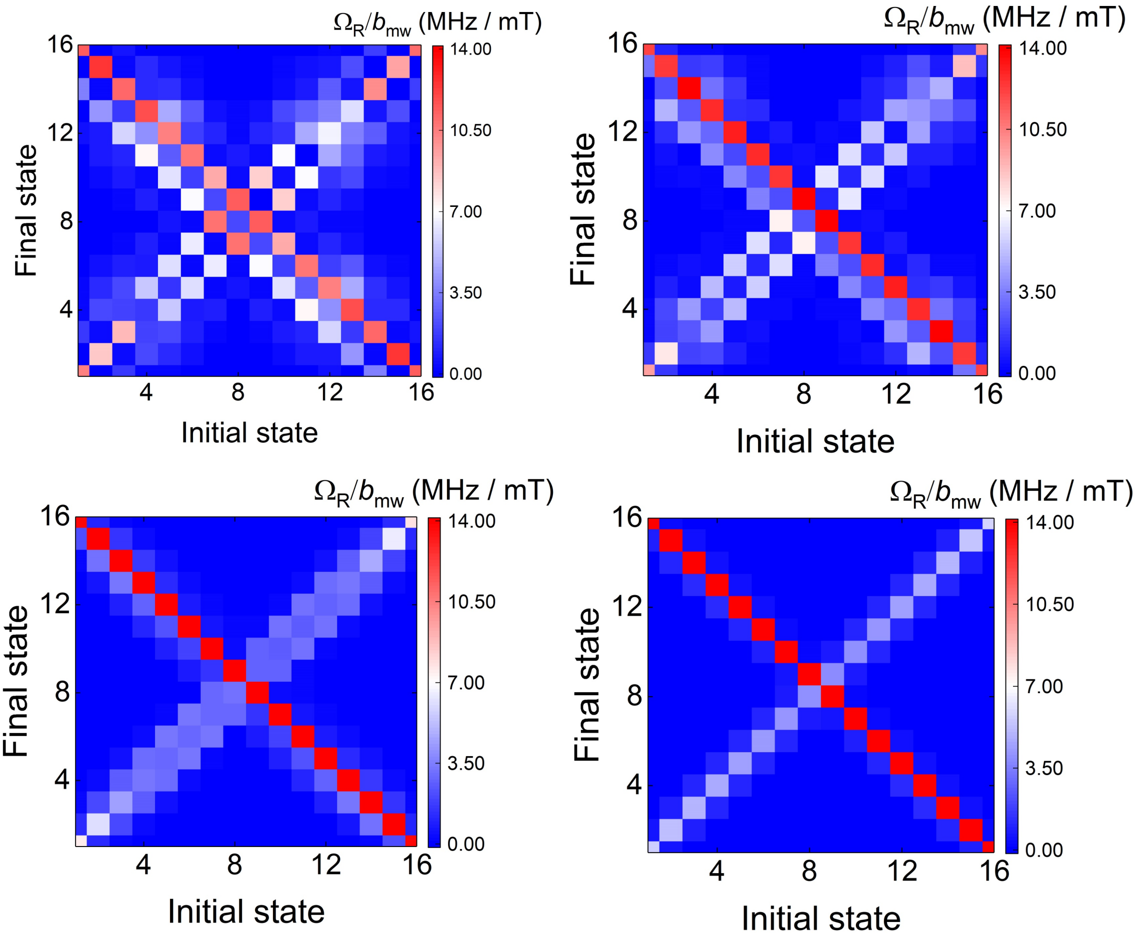

**Figure S33.** Plots of the Rabi frequencies between different electronuclear spin states of [VO(TCPPEt)], calculated from the spin Hamiltonian (Eq. (1) of the main text) and for progressively stronger (from top left to bottom right) magnetic field values *B* = 0.02 T, 0.04 T, 0.1 T and 0.3 T. The field is applied along the X laboratory axis of Fig. S28.

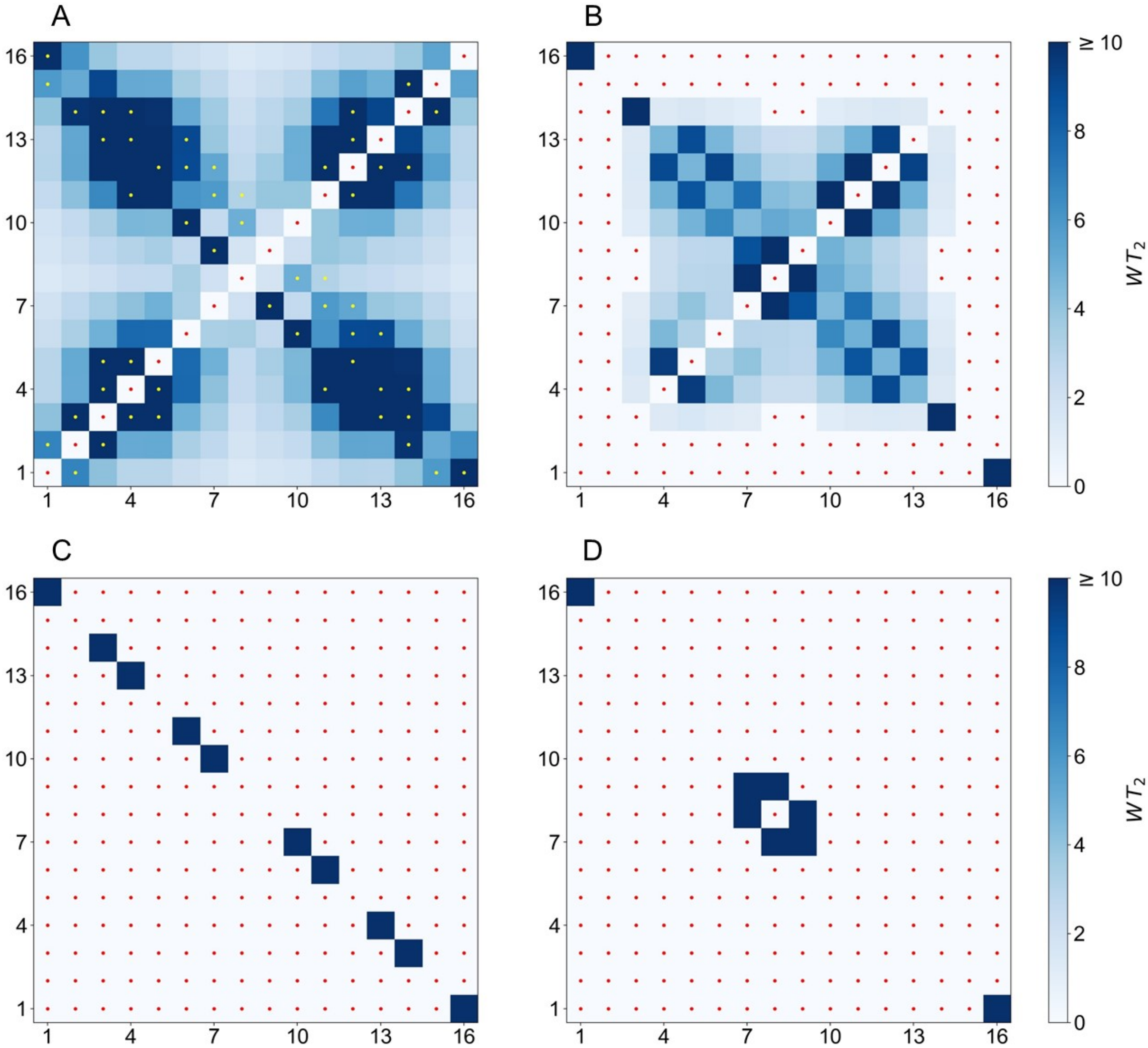

**Figure S34.** Universality plots, showing a 2D map of the operation rates linking different states, of a $S = ½$ and $I = 7/2$ electronuclear spin qudit ($d = 16$). The amplitude of resonant electromagnetic pulses was set to $b_{mw} = 1$ mT and $T_2 = 5$ μs. Yellow dots show the set of resonant transitions that are used to generate all operations. White spots, marked with a red dot at their center, signal pairs of states that cannot be connected by any sequence of such transitions. Panels A and B: calculations performed using the spin Hamiltonian and parameters of $\mathbf{1}^{\mathbf{VO}}$ for, respectively, $B_X = 0.04$ and 0.1 T. Panels C and D: calculations performed for a fully uniaxial ($A_{\|} = 475$ MHz and $A_{\perp} = 0$) and a fully isotropic ($A_{\|} = A_{\perp} = 475$ MHz) hyperfine interaction, respectively.

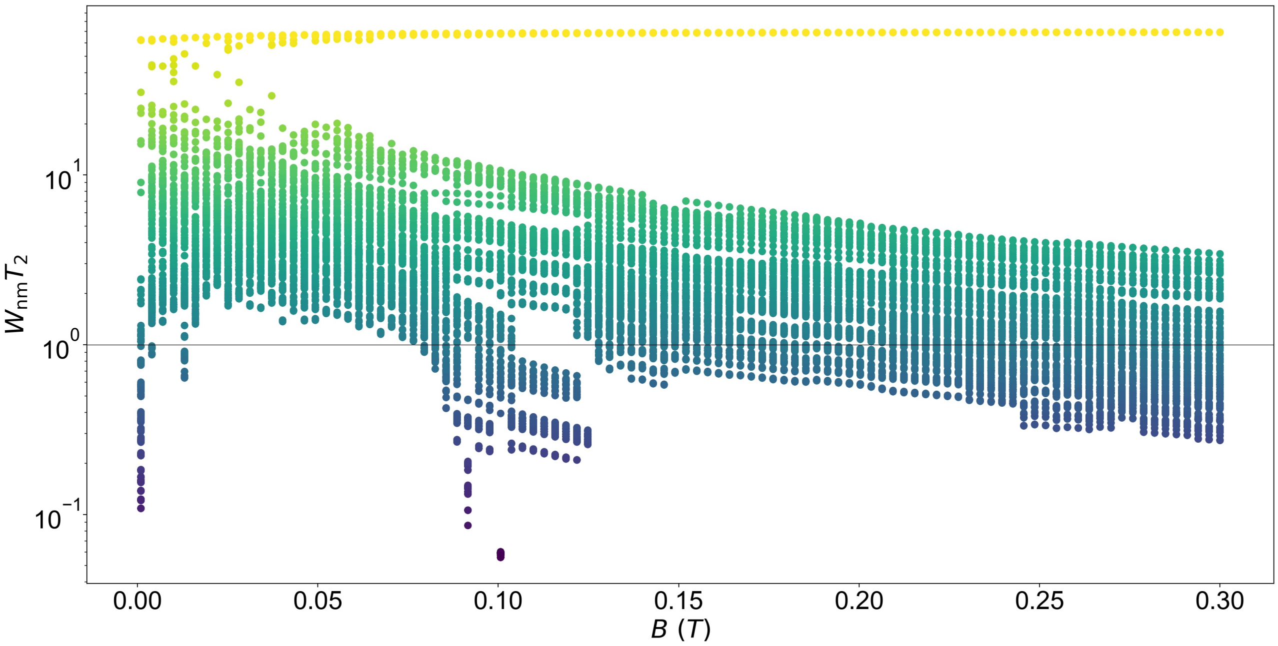

**Figure S35.** Operation rates $W_{\mathrm{nm}}T_2$ between any pair of states of $\mathbf{1^{VO}}$ as a function of $B_X$, showing that more of them become effectively disconnected (for $W_{\mathrm{nm}}T_2 < 1$) with increasing magnetic field. This means that the set of available quantum operations shrinks, thus the system cannot perform universal computations.

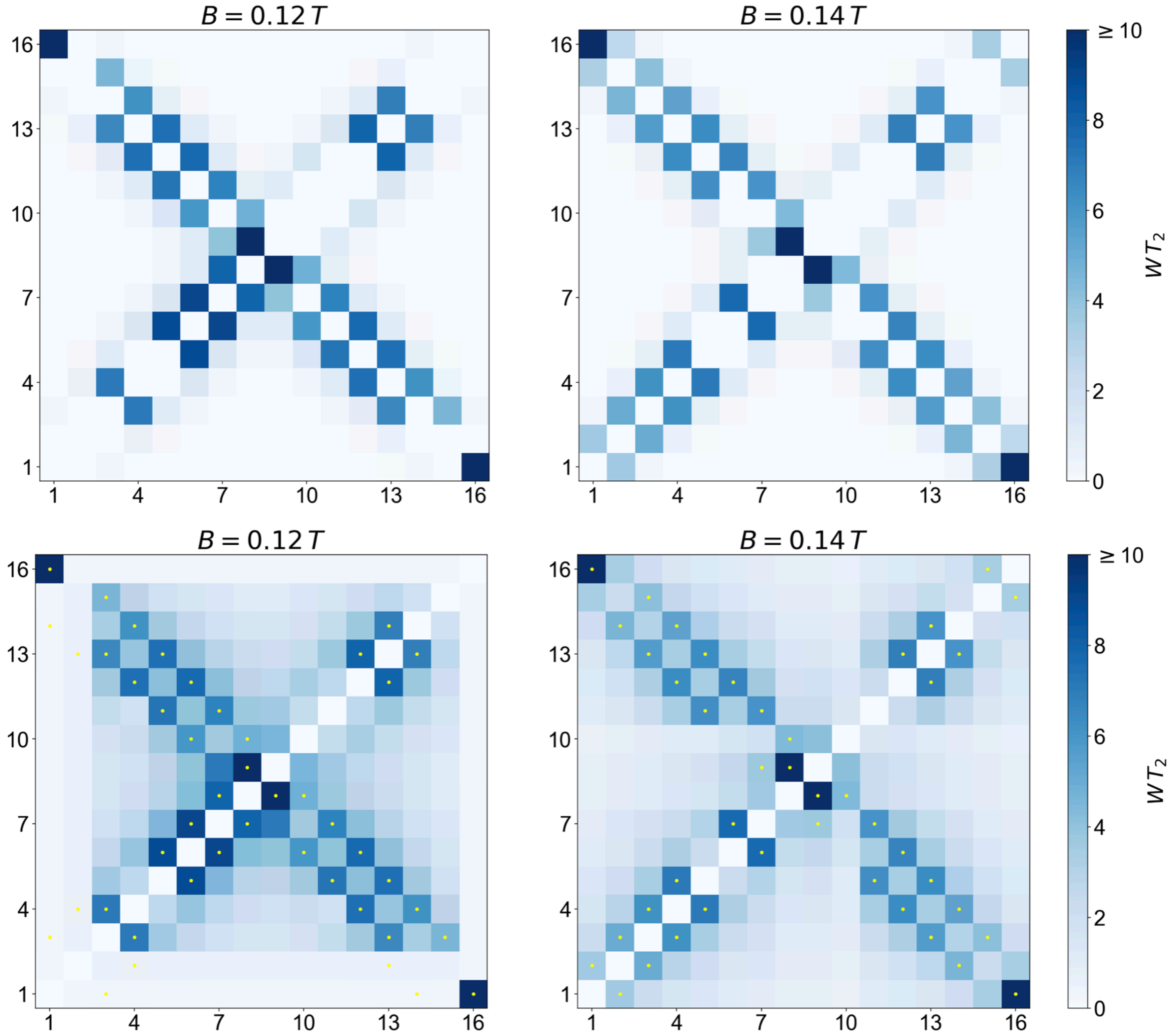

**Figure S36.** Operation rates $W_{\mathrm{nm}}T_2$ between any pair of states of $\mathbf{1}^{\mathbf{VO}}$ at two magnetic fields located just below and above the sudden jump in the minimum $W_{\mathrm{nm}}T_2$ shown in Fig. 8 (bottom panel) of the main text. The two top panels show rates of operations that can be implemented by direct resonant transitions (they are, therefore, Rabi frequencies for such transitions) and that are, at the same time, nondegenerate in frequency with any other (see main text for the quantitative degeneracy criterium). It follows that accidental degeneracies eliminate some resonant transitions at $B_X$ = 0.12 T whereas they are lifted at $B_X$ = 0.14 T. The bottom panels show the universality plots at the same magnetic fields. The fact that some relatively fast transitions are unavailable at 0.12 T imposes that some operations need to be implemented using sequences of slower ones. As a result, the minimum operation rate becomes much smaller.

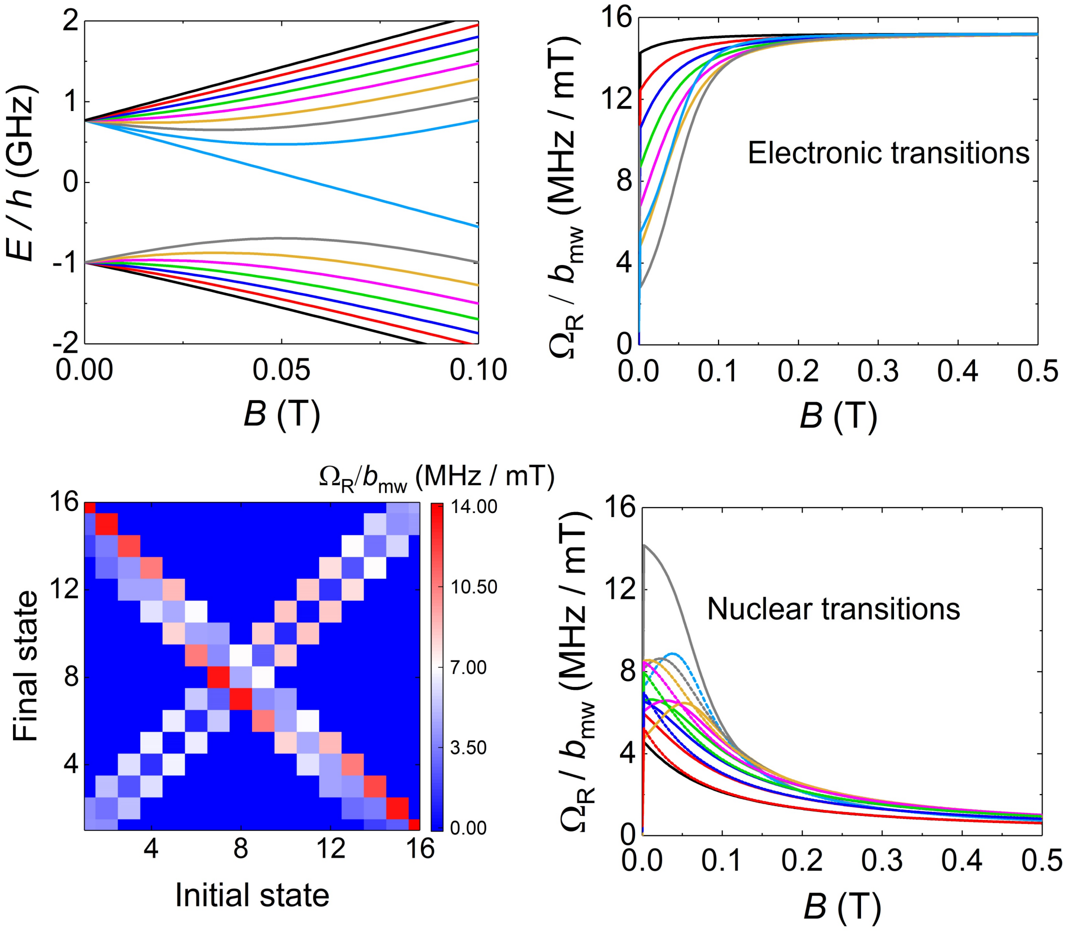

**Figure S37.** Left, top: energy levels of a $S$ = ½ electronic spin coupled to a $I$ = 7/2 nuclear spin coupled by an isotropic hyperfine interaction with $A_{||} = A_{\perp}$ = 475 MHz as a function of magnetic field applied along the X laboratory axis. Left, bottom: colour map of Rabi frequencies for resonant transitions, induced by a microwave magnetic field $b_{mw}$ applied along X, linking different electronuclear spin states at $B_X$ = 0.02 T. Right: Magnetic field dependence of the Rabi frequencies of “electronic” (top) and “nuclear” (bottom) spin transitions.

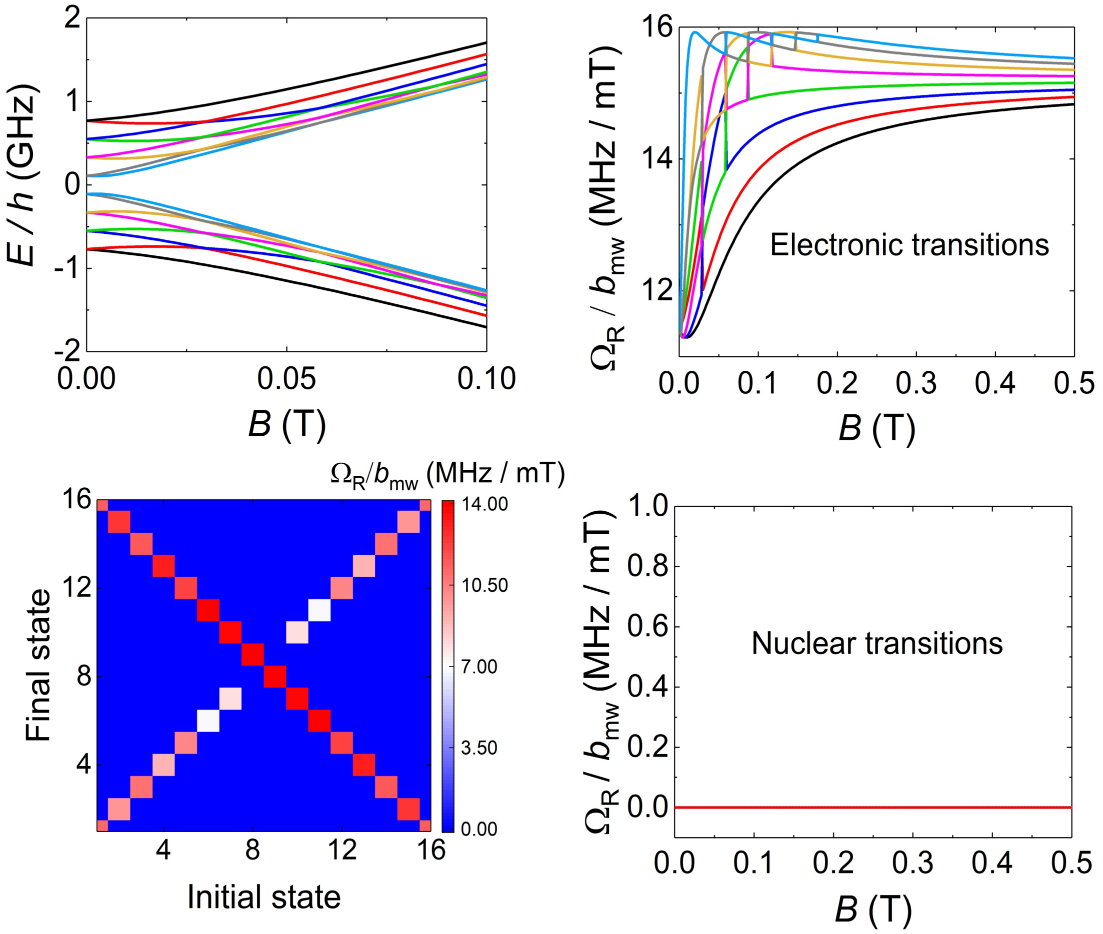

**Figure S38.** Left, top: energy levels of a $S$ = ½ electronic spin coupled to a $I$ = 7/2 nuclear spin by a fully uniaxial hyperfine interaction with $A_{||}$ = 475 MHz and $A_{\perp}$ = 0 as a function of magnetic field applied along the X laboratory axis. Left, bottom: colour map of Rabi frequencies for resonant transitions, induced by a microwave magnetic field $b_{\mathrm{mw}}$ applied along X, linking different electronuclear spin states at $B_X$ = 0.02 T. Right: Magnetic field dependence of the Rabi frequencies of “electronic” (top) and “nuclear” (bottom) spin transitions.